Nuclear energy density optimization

M. Kortelainen,[1,2] T. Lesinski,[1,2] J. Moré,[3] W. Nazarewicz,[1,2,4] J. Sarich,[3] N. Schunck,[1,2] M. V. Stoitsov,[1,2,5] and S. Wild[3]

[1]*Department of Physics and Astronomy, University of Tennessee, Knoxville, Tennessee 37996, USA*

[2]*Physics Division, Oak Ridge National Laboratory, P.O. Box 2008, Oak Ridge, Tennessee 37831, USA*

[3]*Mathematics and Computer Science Division, Argonne National Laboratory, Argonne, Illinois 60439, USA*

[4]*Institute of Theoretical Physics, Warsaw University, ul. Hoża 69, PL-00681 Warsaw, Poland*

[5]*Institute of Nuclear Research and Nuclear Energy, Bulgarian Academy of Sciences, Sofia, Bulgaria*

(Received 27 May 2010; published 13 August 2010)

We carry out state-of-the-art optimization of a nuclear energy density of Skyrme type in the framework of the Hartree-Fock-Bogoliubov theory. The particle-hole and particle-particle channels are optimized simultaneously, and the experimental data set includes both spherical and deformed nuclei. The new model-based, derivative-free optimization algorithm used in this work has been found to be significantly better than standard optimization methods in terms of reliability, speed, accuracy, and precision. The resulting parameter set UNEDF0 results in good agreement with experimental masses, radii, and deformations and seems to be free of finite-size instabilities. An estimate of the reliability of the obtained parameterization is given, based on standard statistical methods. We discuss new physics insights offered by the advanced covariance analysis.

DOI: 10.1103/PhysRevC.82.024313 PACS number(s): 21.60.Jz, 21.10.−k, 21.30.Fe, 21.65.Mn

I. INTRODUCTION

The goal of low-energy nuclear physics is to understand nuclei and how they react. This fascinating science problem is relevant to other fields and to a gamut of societal applications. New vistas have been opened by experimental advances in the production of rare isotopes [1] and new theoretical approaches [2] backed by unprecedented computing power [3]. The rapid experimental developments have resulted in a wealth of unique data from previously unexplored regions of the nuclear landscape. This situation poses a serious challenge to models of nuclear structure and calls for their improved reliability and better-controlled extrapolability.

Theorists seek to formulate a coherent framework for nuclear structure and reactions based on a well-founded microscopic theory that would deliver maximum predictive power with well-quantified uncertainties. To this end, the steady increase in computing power, currently crossing the petaflop barrier, has been beneficial. A paradigm for the new mode of nuclear theory is the US Department of Energy's Scientific Discovery Through Advanced Computing Universal Nuclear Energy Density Functional (UNEDF) project [4], an example of the close alignment of the physics research with the necessary applied mathematics and computer science research.

This study is the fruit of such a partnership, under UNEDF, in which physicists collaborate with mathematicians and computer scientists on a specific science challenge. Our long-term goal in UNEDF is to develop a spectroscopic-quality theoretical framework rooted in the nuclear density functional theory (DFT) [5]. In the first phase of the project, we have developed efficient DFT solvers for the self-consistent Hartree-Fock-Bogoliubov (HFB) problem. Various improvements that we have implemented to carry out large-scale DFT calculations have been recently presented in Refs. [6,7]. These improvements enable comprehensive mass-table calculations, including all even-even nuclei and many different configurations in odd-even and odd-odd nuclei, in less than a day [8,9].

The second phase of the project concerns the development and optimization of the nuclear energy density functional (EDF). Because standard functionals are clearly too restrictive when one is aiming at a quantitative description [10,11], the form of EDF needs to be improved. Novel functionals can be constructed from two- and three-nucleon interactions by using effective field theory and the density matrix expansion technique [12–15] and by using constraints from *ab initio* calculations for very light nuclei and nuclear matter. They can also be obtained by enriching density dependence and adding higher gradient terms in a systematic way [15–17].

Having determined the form of the EDF, one must still optimize the coupling constants of the underlying energy density (ED). Indeed, all energy functionals, irrespective of their theoretical foundations, rely on parameters that must be directly fitted to experimental data. It has been realized recently that high-performance computing can positively impact the optimization strategy. Historically, most nuclear ED parameterizations, such as Skyrme or Gogny, were obtained by a direct fit to selected experimental data from finite nuclei and various nuclear-matter properties (NMPs). Observables commonly included in the fit are binding energies, proton radii, surface thickness, and/or single-particle (s.p.) energies of doubly closed-shell nuclei, as well as NMPs (pseudo-observables) such as energy per particle of infinite and semi-infinite nuclear matter, saturation density, or incompressibility. This is the case, for example, for the SLy4 parameterization of the Skyrme functional of Ref. [18], which we take (somewhat arbitrarily) as a reference point in our study. The D1, D1S, and D1N parameterizations of the Gogny interaction have also been obtained in such a framework [19–21], as well as some parameterizations of relativistic functionals [22,23]. We refer to Refs. [5,24,25] for a more thorough discussion of various fitting strategies and protocols.

In fact, very few examples of EDs are fitted to other types of data. For Skyrme EDFs only, we mention the early attempt of the SkM* parameterization [26], which was

adjusted semiclassically to account for the fission barrier of ^{240}Pu. The Brussels-Montreal set of EDFs has been optimized to data on deformed nuclei, although the actual fit is always performed with a spherical code by using a multistep procedure. For example, in the early versions MSk1–MSk6, the deformation energy of the ground-state configuration was used to renormalize nuclear masses so that the optimization could proceed in spherical symmetry [27]. Similarly, while in the later version HFB14, data on fission barriers were used, the core part of the fitting procedure was carried out in spherical geometry [28]. For SLy4 itself, several parameters were fixed at values empirically expected to yield a correct description of giant resonance energy centroids in random phase approximation (RPA) calculations, although no such calculation was included in the fit nor any quantitative check performed *a posteriori*.

The choice to restrict the data set of observables to those pertaining to nuclear matter and spherical nuclei has almost always been dictated by practical considerations: The cost of performing huge numbers of deformed HFB calculations was deemed too high. It was also rightly argued that the driving terms of the EDF could be pinned down by considering spherical nuclei only. With the need for more precision, however, the limitation to spherical nuclei and NMP is clearly not sufficient. The advent of supercomputers makes it possible to free ourselves from this restriction.

Specifically, the availability of supercomputers has two consequences. First, one can now include in the set of fit observables data corresponding to deformed nuclei, odd-mass systems, excited states, and so forth. More comprehensive data sets should better constrain the various channels of the energy functionals, for example, its deformation or spin-polarization properties. It might soon become possible to directly optimize symmetry-restored EDFs [29], in either a single-reference [30–33] or a multireference [34–36] framework.

In addition, in our quest for improved EDFs, a key step is to understand various constraints imposed by experimental data on ED parameters and the resulting uncertainty margins. Early attempts to use statistical methods of linear-regression and error analysis [37] have been revived recently and applied to determine the correlations among ED parameters, parameter uncertainties, and the errors of calculated observables [10,11,24,25,38]. This approach is essential for providing predictive capability and extrapolability and for estimating the theoretical uncertainties.

The purpose of this work is to revisit the problem of Skyrme ED optimization by (i) removing some of the previous limitations with the help of modern computational resources and (ii) applying regression diagnostics methods on the resulting parameterization. To these ends, we perform functional optimization with a model-based method that is particularly adapted to costly function evaluations, such as when the objective function contains the result of hundreds of symmetry-unrestricted HFB calculations. In our model study, we focus on nuclear masses and radii, with a bias toward heavy nuclei. The final ED parameterization is subjected to a fully fledged correlation and sensitivity analysis. While we do not claim to have found an end-all parameterization of the Skyrme EDF, we believe that the set of techniques we have applied in this study can pave the way to a universal nuclear EDF of spectroscopic quality.

The article is organized as follows. In Sec. II we briefly present the DFT framework used, in particular various parameterizations of the Skyrme EDF and their relations to NMP. We also discuss the choice of experimental observables. Section III presents the specific model-based algorithm used in this work and contains all the technical information related to large-scale HFB calculations. Results are discussed in Sec. IV. Section V contains the conclusions of this work.

II. THEORETICAL FRAMEWORK

This section recalls the features of the Skyrme-DFT theory that are relevant to the optimization problem. A detailed presentation of the theory itself can be found in, for example, Refs. [5,39,40] and references therein. The main focus of the following discussion is on various parameterizations of the Skyrme EDF and the selection of experimental observables chosen to constrain ED parameters.

A. Time-even Skyrme energy density functional

In nuclear DFT, the total energy of the nucleus is given by

$$E = \int \mathcal{H}(\boldsymbol{r}) d^3\boldsymbol{r}, \tag{1}$$

where $\mathcal{H}$ is the local ED that is supposed to be a real, scalar, time-even, and isoscalar function of local densities and their derivatives. The Skyrme ED can be decomposed into the kinetic term, interaction ED χ, pairing ED, Coulomb term, and additional corrections, such as the center-of-mass term. For the kinetic energy term, we set $\hbar^2/2m = 20.73553$ MeV fm^2. The Coulomb Hartree term is calculated exactly, while the exchange term is computed by the Slater approximation. The contribution from the center-of-mass correction has the same structure as the kinetic term and leads to a renormalization of the nucleon mass $1/m \to (1/m)[1 - 1/A]$. All these prescriptions follow the SLy4 parameterization.

The interaction ED can be further decomposed into $\chi = \chi_0 + \chi_1$, with

$$\begin{aligned}\chi_t(\boldsymbol{r}) = {} & C_t^{\rho\rho}\rho_t^2 + C_t^{\rho\tau}\rho_t\tau_t + C_t^{J^2}\boldsymbol{J}_t^2 \\ & + C_t^{\rho\Delta\rho}\rho_t\Delta\rho_t + C_t^{\rho\nabla J}\rho_t\nabla\cdot\boldsymbol{J}_t,\end{aligned} \tag{2}$$

where the isospin index t labels isoscalar ($t = 0$) and isovector ($t = 1$) densities. Because in this work we limit the discussion to even-even nuclei, the terms involving spin, spin-kinetic, and current densities [5,40,41] are absent. The coupling constants $C_t^{\rho\rho}$ contain an additional dependence on the isoscalar density of the form

$$C_t^{\rho\rho} = C_{t0}^{\rho\rho} + C_{t\mathrm{D}}^{\rho\rho}\rho_0^{\gamma}. \tag{3}$$

The standard Skyrme interaction ED therefore contains 13 independent parameters:

$$\left\{C_{t0}^{\rho\rho}, C_{t\mathrm{D}}^{\rho\rho}, C_t^{\rho\Delta\rho}, C_t^{\rho\tau}, C_t^{J^2}, C_t^{\rho\nabla J}\right\}_{t=0,1} \quad \text{and} \quad \gamma. \tag{4}$$

When dealing with the Skyrme interaction EDF (i.e., the functional that originates from the Skyrme interaction), the

coupling constants (4) are uniquely related to the well-known (t,x) parameterization of the Skyrme interaction,

$$\{t_0, t_1, t_2, t_3, x_0, x_1, x_2, x_3, t_o, t_e, b_4, b'_4, \gamma\}. \tag{5}$$

The equations connecting the C and (t,x) parameterization can be found, for example, in Ref. [40].

In this study, nucleonic superconductivity is described by the pairing ED:

$$\breve{\chi}(\boldsymbol{r}) = \sum_{q=n,p} \frac{V_0^q}{2}\left[1 - \frac{1}{2}\frac{\rho(\boldsymbol{r})}{\rho_0}\right]\breve{\rho}^2(\boldsymbol{r}), \tag{6}$$

where $\breve{\rho}$ is the local pairing density and $\rho_0 = 0.16$ fm^{-3} (mixed-pairing prescription [42]).

B. Nuclear-matter properties and Skyrme energy density parameterizations

The (t,x) and C representations are natural parameterizations of the Skyrme EDF, the former in terms of an effective, density-dependent two-body interaction and the latter as a general functional of the density. However, these representations do not provide a straightforward connection to physical observables; hence, it is not immediately obvious what the search range for these parameters should be. It is therefore advantageous to relate them to fundamental properties of symmetric and asymmetric homogeneous nuclear matter, which have a clear physical interpretation and the range of which is known [25,43,44].

The starting point in the discussion of NMPs is the equation of state (EOS) of the infinite homogeneous nuclear matter: $E/A = W(\rho_n, \rho_p)$. The Coulomb energy is disregarded, all gradient terms vanish, and the kinetic ED is replaced by its Thomas-Fermi expression. Assuming an unpolarized system, one can also ignore terms involving time-odd spin densities and currents.

The expansion of $W(\rho_n, \rho_p)$ around the equilibrium density ρ_c and $I = 0$ can be written as

$$W(\rho_n, \rho_p) = W(\rho_0, I) = W(\rho_0) + S_2(\rho_0)I^2 + \mathcal{O}(I^4), \tag{7}$$

where $I = \rho_1/\rho_0 = (\rho_n - \rho_p)/\rho_0$ is the relative neutron excess, $\rho_0 = \rho_n + \rho_p$, $\rho_1 = \rho_n - \rho_p$,

$$W(\rho_0) = \frac{E^{\rm NM}}{A} + \frac{P^{\rm NM}}{\rho_c^2}(\rho_0 - \rho_c) + \frac{K^{\rm NM}}{18\rho_c^2}(\rho_0 - \rho_c)^2, \tag{8}$$

and

$$S_2(\rho_0) = a_{\rm sym}^{\rm NM} + \frac{L_{\rm sym}^{\rm NM}}{3\rho_c}(\rho_0 - \rho_c) + \frac{\Delta K^{\rm NM}}{18\rho_c^2}(\rho_0 - \rho_c)^2. \tag{9}$$

In these equations, $E^{\rm NM}/A$ stands for the total energy per nucleon at equilibrium, $P^{\rm NM}$ represents the nucleonic pressure, $K^{\rm NM}$ is the nuclear-matter incompressibility, $a_{\rm sym}^{\rm NM}$ is the symmetry energy coefficient, $L_{\rm sym}^{\rm NM}$ represents the density dependence of the symmetry energy, and $\Delta K^{\rm NM}$ is a correction to the incompressibility.

1. Symmetric nuclear matter

In the regime of symmetric nuclear matter (SNM), $\rho_{\rm n} = \rho_{\rm p} = \rho_0/2$ and $I = 0$, which eliminates all isovector terms. The isoscalar kinetic ED per particle is

$$\tau_0 = C_{\rm k}\rho_0^{2/3},\ C_{\rm k} = \frac{3}{5}\left(\frac{3\pi^2}{2}\right)^{2/3}. \tag{10}$$

The nuclear-matter saturation curve $W(\rho_0)$ is expected to have the following properties:

$$\rho_c \approx 0.16\ \text{fm}^{-3}, \tag{11}$$

$$P^{\rm NM} = \rho^2\frac{dW(\rho_0)}{d\rho_0}\bigg|_{\rho_0=\rho_c} = 0, \tag{12}$$

$$\frac{E^{\rm NM}}{A} = W(\rho_c) \approx -16\ \text{MeV}. \tag{13}$$

The value of the incompressibility modulus is related to the centroid energies of giant isoscalar monopole resonances in isospin-symmetric nuclei [45] and is expected to be [46,47]

$$K^{\rm NM} = 9\rho_0^2\frac{d^2W(\rho_0)}{d\rho_0^2}\bigg|_{\rho_0=\rho_c} \approx 220 \pm 10\ \text{MeV}, \tag{14}$$

with a strong preference for 230 MeV [48]. Another important NMP, entering the SNM EOS indirectly, is the isoscalar effective mass

$$M_s^{*-1} = \frac{2m}{\hbar^2}\frac{dE}{d\tau_0}\bigg|_{\rho_0=\rho_c}, \tag{15}$$

which quantifies the momentum-dependence of the mean field and drives the density of the s.p. spectrum. An appropriate value for a fit to experimental s.p. energies is $M_s^* = 1$ [49], while *ab initio* calculations performed at the Brueckner-Hartree-Fock level in infinite nuclear matter suggest a slightly lower value for the Landau (Fermi-level) effective mass extracted from the on-shell s.p. spectrum [50–53]. Mass fits also seem to favor a value close to unity, although significant freedom exists [54].

The SNM EOS expressed in terms of the coupling constants of the Skyrme EDF is

$$W(\rho_0) = \left(\frac{\hbar^2}{2m} + C_0^{\rho\tau}\rho_0\right)C_{\rm k}\rho_0^{2/3} + \left(C_{00}^{\rho\rho} + C_{0D}^{\rho\rho}\rho_0^{\gamma}\right)\rho_0. \tag{16}$$

Computing the quantities (13)–(15) using Eq. (16) allows us to express the coupling constants $C_{00}^{\rho\rho}$, $C_{0D}^{\rho\rho}$, and $C_0^{\rho\tau}$ and the power γ in terms of $E^{\rm NM}/A$, $P^{\rm NM} = 0$, $K^{\rm NM}$, and M_s^{*-1}. The resulting expressions are [43] as follows:

$$C_{00}^{\rho\rho} = \frac{1}{3\gamma\rho_c}\left\{\frac{\hbar^2}{2m}\left[(2-3\gamma)M_s^{*-1} - 3\right]\tau_c + 3(1+\gamma)\frac{E^{\rm NM}}{A}\right\}, \tag{17}$$

$$C_{0D}^{\rho\rho} = \frac{1}{3\gamma\rho_c^{1+\gamma}}\left[\frac{\hbar^2}{2m}\left(3 - 2M_s^{*-1}\right)\tau_c - 3\frac{E^{\rm NM}}{A}\right], \tag{18}$$

$$C_0^{\rho\tau} = \frac{\hbar^2}{2m}\left(M_s^{*-1} - 1\right)\frac{1}{\rho_c}, \tag{19}$$

$$\gamma = \frac{\frac{\hbar^2}{2m}\left(4M_s^{*-1}-3\right)\tau_c - K^{\rm NM} - 9\frac{E^{\rm NM}}{A}}{\frac{\hbar^2}{2m}\left(6M_s^{*-1}-9\right)\tau_c + 9\frac{E^{\rm NM}}{A}}, \tag{20}$$

where $\tau_c = C_{\rm k}\rho_c^{2/3}$.

2. Asymmetric nuclear matter

In asymmetric nuclear matter (ANM), neutron and proton densities are different, and isovector terms are nonzero. The local and kinetic energy densities are

$$\rho_1 = I\rho_0, \tag{21}$$

$$\tau_0 = C_{\rm k}\rho_0^{2/3}F_+(I), \tag{22}$$

$$\tau_1 = C_{\rm k}\rho_0^{2/3}F_-(I), \tag{23}$$

$$F_\pm(I) = \tfrac{1}{2}[(1+I)^{5/3} \pm (1-I)^{5/3}]. \tag{24}$$

The nuclear-matter EOS $W(I,\rho)$ now depends on the relative neutron excess I. The most important parameter characterizing the isospin dependence of the ANM EOS is the symmetry energy at saturation density,

$$S_2(\rho_{\rm c}) = a_{\rm sym}^{\rm NM} = \frac{1}{2}\frac{d^2W(\rho_0,I)}{dI^2}\bigg|_{\substack{\rho_0=\rho_{\rm c}\\ I=0}}. \tag{25}$$

The value of $S_2(\rho_{\rm c})$ varies from 28 to 36 MeV among EDFs extrapolated to nuclear matter [44,55]. It is understood [56,57] that nuclear masses constrain a combination of the symmetry and surface-symmetry energy parameters in a given EDF, and this fact explains the large spread of values.

The variation of the density-dependent symmetry energy S_2 with ρ_0 is usually parameterized through

$$L_{\rm sym}^{\rm NM} = 3\rho_{\rm c}\left.\frac{dS_2(\rho_0)}{d\rho_0}\right|_{\rho_0=\rho_{\rm c}}, \tag{26}$$

the value of which appears correlated with the thickness of neutron skins in asymmetric nuclei (see Ref. [38] and references therein). An empirical determination of this parameter yields $L_{\rm sym}^{\rm NM} = 80 \pm 30$ MeV [58,59]. One now introduces

$$\Delta K^{\rm NM} = 9\rho_{\rm c}^2\left.\frac{d^2S_2(\rho_0)}{d^2\rho_0}\right|_{\rho_0=\rho_{\rm c}}, \tag{27}$$

which affects the incompressibility of the ANM and thus the isoscalar monopole resonance energies in neutron-rich nuclei [45]. For the SLy4 EDF, the values of the last two parameters were determined by the fit to the neutron-matter EOS. We let these quantities be constrained by our experimental data set. We see whether these data leave enough freedom to apply additional constraints in the regression analysis.

The momentum dependence of the mean field is also affected by isospin: Neutron and proton effective masses are different in asymmetric matter [60], an effect quantified by the isovector effective mass

$$M_v^{*-1} = M_s^{*-1} - \frac{2m}{\hbar^2}\left.\frac{dE}{d\tau_1}\right|_{\substack{\rho_0=\rho_{\rm c}\\ I=0}}. \tag{28}$$

The EOS of homogeneous ANM can be written as

$$W(I,\rho_0) = \left(\frac{\hbar^2}{2m} + C_0^{\rho\tau}\rho\right)C_{\rm k}\rho_0^{2/3}F_+(I) + C_1^{\rho\tau}C_{\rm k}\rho_0^{5/3}IF_-(I) + \left[C_{00}^{\rho\rho} + C_{0D}^{\rho\rho}\rho_0^{\gamma} + I^2\left(C_{10}^{\rho\rho} + C_{1D}^{\rho\rho}\rho_0^{\gamma}\right)\right]\rho_0. \tag{29}$$

Just as for SNM, we compute the quantities (25)–(28) from Eq. (29) and obtain an expression for $C_1^{\rho\tau}$, $C_{10}^{\rho\rho}$, and $C_{1D}^{\rho\rho}$ [43]:

$$C_1^{\rho\tau} = C_0^{\rho\tau} - \frac{\hbar^2}{2m}\left(M_v^{*-1}-1\right)\frac{1}{\rho_{\rm c}}, \tag{30}$$

$$C_{10}^{\rho\rho} = \frac{1}{27\gamma\rho_{\rm c}}\Bigg[27(1+\gamma)a_{\rm sym}^{\rm NM} - 9L_{\rm sym}^{\rm NM} + 5\tau_c(2-3\gamma) \times \left(C_0^{\rho\tau} + 3C_1^{\rho\tau}\right)\rho_{\rm c} - 5\tau_c(1+3\gamma)\frac{\hbar^2}{2m}\Bigg], \tag{31}$$

$$C_{1D}^{\rho\rho} = \frac{1}{27\gamma\rho_{\rm c}^{\gamma+1}}\Bigg[-27a_{\rm sym}^{\rm NM} + 9L_{\rm sym}^{\rm NM} + 5\left(\frac{\hbar^2}{2m} - 2\rho_{\rm c}\left(C_0^{\rho\tau} + 3C_1^{\rho\tau}\right)\right)\tau_c\Bigg]. \tag{32}$$

Using relations (20)–(32), we express 7 of the original 13 parameters (4) of the Skyrme EDF as functions of NMPs. The remaining 6 are not known exactly and should therefore not be used as rigid constraints [25]. However, the expected values of all these NMPs are sufficient to provide well-defined intervals of variation during the optimization process. The 6 remaining coupling constants are the isoscalar and isovector $C_t^{\rho\Delta\rho}$, spin-orbit $C_t^{\rho\nabla J}$, and tensor $C_t^{J^2}$ terms. Consequently, the Skyrme EDF depends on the following 13 parameters:

$$\{\rho_{\rm c}, E^{\rm NM}/A, M_s^*, K^{\rm NM}, a_{\rm sym}^{\rm NM}, L_{\rm sym}^{\rm NM}, M_v^*, C_0^{\rho\Delta\rho}, C_1^{\rho\Delta\rho}, C_0^{\rho\nabla J}, C_1^{\rho\nabla J}, C_0^{J^2}, C_1^{J^2}\}. \tag{33}$$

C. Fit observables

To calibrate the EDF, we selected a pool of fit observables that constitute the UNEDF experimental database [61]. The purpose of the database is to provide a standard and comprehensive set of experimental data that can be used to systematically optimize EDFs. Because we wish to provide, together with the optimized set of parameters, a measure of its intrinsic quality via the error and sensitivity analysis, for every observable an error bar should also be defined. We organized our database into three major categories—spherical, deformed, and symmetry-unrestricted—which reflect the level of symmetry breaking of the underlying EDF and thereby the complexity of its numerical implementation. More details can be found in Ref. [61].

The focus of this work is on a well-controlled optimization methodology, and the emphasis is on global nuclear properties such as masses and proton radii. Our functional is therefore restricted to time-even densities, and only spherical or axially deformed nuclei are considered. The chosen observables embrace data for 72 nuclei, which are proven to allow a reasonable DFT description. The selected experimental data set is presented in Fig. 1. As can be seen, the emphasis is on the heavy nuclei. Indeed, there are only 11 nuclei with $A < 66$

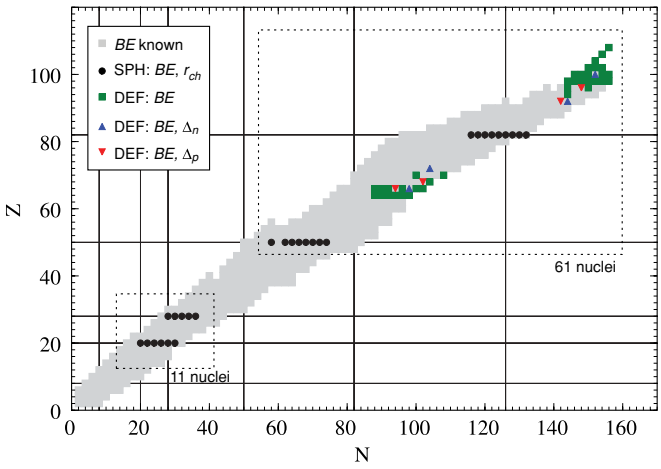

FIG. 1. (Color online) Experimental set of fit observables used in this work. The set contains data for 11 nuclei with $A < 66$ and 61 nuclei with $A > 106$.

in our data set. In what follows, we give a detailed description of the set of fit observables used in this work.

1. Deformed nuclei

In our optimization, we considered binding energies of 44 well-deformed even-even nuclei shown in Table I. Candidates were selected from an HFB mass-table calculation with the SLy4 parameterization requiring that their ground-state equilibrium deformation be greater than $|\beta| = 0.25$. Because the majority of atomic nuclei are deformed in their ground states, by including binding energies of deformed systems in the database, one hopes to better probe the surface properties of the EDF.

TABLE I. Nuclear binding energies (in MeV; the electronic energy correction has been subtracted) [62] for the 44 deformed nuclei selected in this work. The columns marked "No." are the data-point numbers.

No.	Z	N	E	No.	Z	N	E
1	108	156	−1925.697	23	94	144	−1800.523
2	106	154	−1908.038	24	92	144	−1789.701
3	104	152	−1889.709	25	92	142	−1777.858
4	102	154	−1897.729	26	90	142	−1766.015
5	102	152	−1884.685	27	72	104	−1418.407
6	102	150	−1870.386	28	70	108	−1431.260
7	100	156	−1901.673	29	70	100	−1377.760
8	100	154	−1890.112	30	68	104	−1391.213
9	100	152	−1878.056	31	68	102	−1378.695
10	100	150	−1864.657	32	66	102	−1362.591
11	100	148	−1850.682	33	66	100	−1350.474
12	100	146	−1836.305	34	66	98	−1337.714
13	98	156	−1891.281	35	66	96	−1323.785
14	98	154	−1880.445	36	66	94	−1309.134
15	98	152	−1869.165	37	66	92	−1293.725
16	98	150	−1856.954	38	66	90	−1277.701
17	98	148	−1843.959	39	64	98	−1321.473
18	98	146	−1830.429	40	64	96	−1308.992
19	98	144	−1816.428	41	64	94	−1295.597
20	96	150	−1847.037	42	64	92	−1281.300
21	96	148	−1835.059	43	64	90	−1266.329
22	96	144	−1809.502	44	64	88	−1251.187

TABLE II. Nuclear binding energies (in MeV; the electronic energy correction has been subtracted) [65] for 28 spherical nuclei selected in this work. The columns marked "No." are the data-point numbers.

No.	Z	N	E	No.	Z	N	E
45	82	132	−1662.762	59	50	64	−971.406
46	82	130	−1653.988	60	50	62	−953.335
47	82	128	−1645.030	61	50	58	−914.424
48	82	126	−1635.909	62	28	36	−561.714
49	82	124	−1621.803	63	28	34	−545.217
50	82	122	−1606.984	64	28	32	−526.801
51	82	120	−1591.666	65	28	30	−506.459
52	82	118	−1575.833	66	28	28	−483.949
53	82	116	−1559.483	67	20	30	−427.473
54	50	74	−1049.835	68	20	28	−415.972
55	50	72	−1035.365	69	20	26	−398.751
56	50	70	−1020.375	70	20	24	−380.942
57	50	68	−1004.785	71	20	22	−361.877
58	50	66	−988.535	72	20	20	−342.033

2. Spherical nuclei

Table II lists the nuclear masses of a selected set of 28 spherical nuclei considered in the fit. In these nuclei, correlations beyond mean field are expected to be relatively constant [25]. Because the list includes doubly magic nuclei, it should provide strong constraints, as these nuclei tend to deviate from global mass trends [10]. Moreover, the masses of ^{40}Ca, ^{48}Ca, and ^{56}Ni help constrain the spin-orbit term [60,63,64]. All the masses of spherical and deformed nuclei given in Tables I and II have been corrected for the electronic binding energy. The nuclear binding energy $E_{\rm nuc}(Z,N)$ is given by

$$E_{\rm nuc}(Z,N) = E_{\rm ato}(Z,N) - E_{\rm el}, \tag{34}$$

where $E_{\rm ato}(Z,N)$ is the atomic binding energy and $E_{\rm el} = -1.433 \times 10^{-5} Z^{2.39}$MeV.

For the same 28 spherical nuclei, we also consider the proton rms point radius $\langle R_{\rm p}^2 \rangle$, which we extract from the charge radius $\langle R_{\rm ch}^2 \rangle$ of Ref. [66] using the standard relation

$$\langle R_{\rm ch}^2 \rangle = \langle R_{\rm p}^2 \rangle + \langle r_{\rm p}^2 \rangle + \frac{N}{Z} \langle r_{\rm n}^2 \rangle, \tag{35}$$

where the proton charge radius, $\sqrt{\langle r_{\rm p}^2 \rangle} = 0.877$ fm, and the neutron charge radius, $\langle r_{\rm n}^2 \rangle = -0.1161$ fm^2, were taken from Ref. [67]. The values of proton radii used in this work are listed in Table III.

TABLE III. Proton rms radii (in fm) [66] for the 28 spherical nuclei selected in this work. The columns marked "No." are the data-point numbers.

No.	Z	N	r_p	No.	Z	N	r_p
73	82	132	5.506	87	50	64	4.542
74	82	130	5.488	88	50	62	4.527
75	82	128	5.469	89	50	58	4.492
76	82	126	5.450	90	28	36	3.787
77	82	124	5.439	91	28	34	3.765
78	82	122	5.428	92	28	32	3.733
79	82	120	5.418	93	28	30	3.689
80	82	118	5.403	94	28	28	3.661
81	82	116	5.394	95	20	30	3.437
82	50	74	4.609	96	20	28	3.390
83	50	72	4.598	97	20	26	3.412
84	50	70	4.586	98	20	24	3.432
85	50	68	4.573	99	20	22	3.420
86	50	66	4.558	100	20	20	3.382

3. Pairing

Because the particle-hole and particle-particle channels cannot easily be disentangled, we must also include observables that will help us pin down the magnitude of pairing correlations. Usually, the pairing part of the EDF is constrained by considering the odd-even staggering (OES) of binding energy (see Ref. [68] for a recent survey). Additional constraints on the pairing ED may be imposed by taking calculated pairing gaps in SNM and neutron matter [69]. This strategy has been adopted by the Brussels-Montreal group in their most recent model HFB-17 [70].

In this work, we constrain pairing EDF by means of the OES defined by a three-point formula $\Delta^{(3)}$ [68,71]. As customary, the theoretical result for even particle number N is compared with the experimental $\Delta^{(3)}$ for $N+1$ [72]. We took four values of $\Delta^{(3)}$ for neutrons and four for protons(see Table IV). All these nuclei belong to the deformed set of Table I. Our choice has been motivated by the observation that fitting pairing properties in spherical systems, where the level density is much greater, may lead to an underestimation of the overall pairing strength [68].

With the fairly simple pairing ED (6) that we use, it is not essential to require very high precision for the OES. For that reason, to be free from local fluctuations, we chose in each even-even nucleus the average over the two even-odd or odd-even isotopes: $\tilde{\Delta}_n^{(3)}(N) = [\Delta^{(3)}(N-1) + \Delta^{(3)}(N+1)]/2$. Including average values of $\tilde{\Delta}^{(3)}$ in our data set ensures that the magnitude of pairing correlations is correct and remains such throughout the fitting procedure. Theoretical OES values have been computed from the average HFB pairing gap [73,74].

TABLE IV. Values of the neutron and proton average odd-even mass staggering (in MeV) considered in this work. The columns marked "No." are the data-point numbers.

Neutrons				Protons			
No.	Z	N	$\tilde{\Delta}_n^{(3)}$	No.	Z	N	$\tilde{\Delta}_p^{(3)}$
101	100	152	0.515	105	96	148	0.566
102	92	144	0.569	106	92	142	0.606
103	72	104	0.675	107	68	102	0.504
104	66	98	0.679	108	66	94	0.728

III. OPTIMIZATION ALGORITHM

This section briefly presents the new algorithm used in our optimization. We refer to it by the acronym POUNDERS, standing for Practical Optimization Using No Derivatives (for Squares). We also provide the numerical parameters used in the HFB calculations, and we give the characteristics of the objective function used in the optimization.

A. Derivative-free optimization method

To outline our algorithm, we adopt the following notation. We denote the set of parameters and coupling constants of the Skyrme EDF to be fitted by $\mathbf{x} \in \mathbb{R}^{n_x}$, where n_x is the number of coupling constants of components x_k to fit. We define a composite fit function made of D_T different types of data: nuclear masses, proton radii, and so on. The number n_i of data points for a given type i may vary; for example, we have more masses than rms radii. The output of the calculation for type i is denoted by $s_{i,j}(\mathbf{x})$ for nucleus j and obviously depends on the parameterization of the functional, that is, the vector $\mathbf{x} \in \mathbb{R}^{n_x}$. For type i and nucleus j, the experimental value of a given observable is denoted $d_{i,j}$.

While many objectives are possible, we minimize the weighted sum of squared errors

$$\chi^2(\mathbf{x}) = \frac{1}{n_d - n_x} \sum_{i=1}^{D_T} \sum_{j=1}^{n_i} \left(\frac{s_{i,j}(\mathbf{x}) - d_{i,j}}{w_i} \right)^2, \qquad (36)$$

where $n_d = \sum_{i=1}^{D_T} n_i$ denotes the total number of data points being fit. The weights $w_i > 0$ render the type i difference dimensionless and are chosen to balance the goals of fitting different observable types simultaneously.

The objective Eq. (36) is a special case of the nonlinear least-squares function,

$$f(\mathbf{x}) = \frac{1}{2} \sum_{i=1}^{n_d} F_i(\mathbf{x})^2 = \frac{1}{2} \|\mathbf{F}(\mathbf{x})\|^2, \qquad (37)$$

where the function $\mathbf{F} : \mathbb{R}^{n_x} \to \mathbb{R}^{n_d}$ yields the vector of reduced errors. Most optimization approaches to minimizing Eq. (37) are based on Newton's method, whereby f is replaced by its second-order expansion,

$$f(\mathbf{x}+\boldsymbol{\delta}) \approx f(\mathbf{x}) + \boldsymbol{\delta}^T J(\mathbf{x})^T \mathbf{F}(\mathbf{x}) + \frac{1}{2} \boldsymbol{\delta}^T \times \left(J(\mathbf{x})^T J(\mathbf{x}) + \sum_{i=1}^{n_d} F_i(\mathbf{x}) \nabla^2 F_i(\mathbf{x}) \right) \boldsymbol{\delta}, \qquad (38)$$

where $\boldsymbol{\delta} \in \mathbb{R}^{n_x}$ and $J(\mathbf{x})$ is the Jacobian matrix $J(\mathbf{x}) = [\nabla F_1(\mathbf{x}), \ldots, \nabla F_{n_d}(\mathbf{x})]^T$.

In the problem at hand (and many others), the derivatives of $F_i(\mathbf{x})$ with respect to $\mathbf{x}$, $\nabla F_i(\mathbf{x})$ and $\nabla^2 F_i(\mathbf{x})$, exist for virtually all $\mathbf{x}$, but their calculation for use in the optimization is impractical. Indeed, although derivatives of binding energies can be obtained through the Feynman-Hellman theorem, other observables such as radii would require the use of perturbation theory or a cumbersome and potentially imprecise calculation of numerical differences. In such a case, the optimization algorithm must be *derivative-free*, relying only on the function value outputs $\mathbf{F}(\mathbf{x})$. Popular algorithms in this setting include the Nelder-Mead (N-M) method and other direct search algorithms [75] and genetic algorithms and other heuristics [76]. However, a recent benchmarking study [77] found that methods that form a smooth approximation model of the objective to exploit the smoothness and structure of the objective may be able to obtain better solutions in fewer evaluations.

In the case of nonlinear least squares, we follow the approach of forming a quadratic model for each component,

$$q_i(\mathbf{x}+\boldsymbol{\delta}) = F_i(\mathbf{x}) + \boldsymbol{\delta}^T \mathbf{g}_i + \tfrac{1}{2}\boldsymbol{\delta}^T \mathbf{H}_i \boldsymbol{\delta}, \tag{39}$$

with $\mathbf{g}_i$ and $\mathbf{H}_i = \mathbf{H}_i^T$ playing the role of the unknown derivatives $\nabla F_i(\mathbf{x})$ and $\nabla^2 F_i(\mathbf{x})$, respectively. We obtain the model parameters $\mathbf{g}_i$ and $\mathbf{H}_i$ by requiring that the model q_i agree with the true function F_i on a set $\mathcal{X}$ of $\mathbf{x}$ values at which F_i is known. Mathematically, these parameters are solutions to the convex quadratic program

$$\min_{\mathbf{g}_i,\mathbf{H}_i}\{\|\mathbf{H}_i\|_F : q_i(\mathbf{x}_k) = F_i(\mathbf{x}_k) \quad \forall \mathbf{x}_k \in \mathcal{X}\}, \tag{40}$$

where $\|\|_F$ is the Frobenius norm and the interpolation set $\mathcal{X}$ contains between n_x+1 and $(n_x+1)(n_x+2)/2$ points satisfying geometric conditions detailed in Refs. [78,79].

The quadratic model q_i cannot be expected to approximate F_i at $\mathbf{x}$ values far from the points in $\mathcal{X}$. Hence, we use a trust region framework, whereby the model q_i is trusted only close to a base-point $\hat{\mathbf{x}}$. Given a radius $\Delta > 0$, we let $\mathcal{B} = \{\mathbf{x} \in \mathbb{R}^{n_x} : \|\mathbf{x}-\hat{\mathbf{x}}\| \leqslant \Delta\}$ denote the spherical neighborhood within which we trust q_i. Correspondingly, the interpolation points in $\mathcal{X}$ should not be too far away from $\mathcal{B}$.

Provided that we know the entire vector of observables $\mathbf{F}(\mathbf{x}_k)$ at each $\mathbf{x}_k \in \mathcal{X}$, we can obtain a set of model parameters $\{(\mathbf{g}_i, \mathbf{H}_i)\}_{i=1}^{n_d}$, which we trust inside a common region $\mathcal{B}$ centered about $\hat{\mathbf{x}}$. We can thus form a derivative-free model of the quadratic Eq. (38),

$$m(\hat{\mathbf{x}}+\boldsymbol{\delta}) = f(\hat{\mathbf{x}}) + \boldsymbol{\delta}^T \sum_{i=1}^{n_d} F_i(\hat{\mathbf{x}})\mathbf{g}_i + \frac{1}{2}\boldsymbol{\delta}^T \sum_{i=1}^{n_d} \left[\mathbf{g}_i \mathbf{g}_i^T + F_i(\hat{\mathbf{x}})\mathbf{H}_i\right]\boldsymbol{\delta}. \tag{41}$$

Because we trust this model within $\mathcal{B}$, we expect that a better $\mathbf{x}$ can be obtained by solving the trust region subproblem $\min_\delta\{m(\hat{\mathbf{x}}+\boldsymbol{\delta}) : \hat{\mathbf{x}}+\boldsymbol{\delta} \in \mathcal{B}\}$. This problem minimizes a quadratic with known derivatives over a compact, convex region and is hence decidedly easier than the original problem. The observables are then evaluated at the solution to this subproblem so that we obtain $\mathbf{F}(\hat{\mathbf{x}}+\boldsymbol{\delta})$.

An iterative Newton-like procedure is thus obtained. We note that the trust region radius Δ grows and shrinks from one iteration to the next depending on the ratio of the actual decrease obtained at the new point versus the decrease predicted by the model in Eq. (41). Similarly, our current estimate of the solution, $\hat{\mathbf{x}}$, is changed only if an adequate decrease of the function was obtained or if we achieved a simple decrease in the function value and the geometry of the interpolation set $\mathcal{X}$ gives us confidence. If we did not adequately decrease f, we must evaluate at an additional $\mathbf{x}$ value to improve the geometry of the set $\mathcal{X}$ in subsequent iterations.

B. Numerical parameters

The evaluation of the function (36) at point $\mathbf{x}$ requires 72 HFB calculations to generate the $s_{i,j}(\mathbf{x})$ points for the 72 nuclei j taken in the data set. All HFB calculations were performed with the code HFBTHO [80]. This code solves the Skyrme-HFB equations in the harmonic oscillator basis assuming axial and reflection symmetry. In our optimization, we used a spherical basis of $N_{\text{shell}} = 20$. The oscillator frequency was determined for a given nucleus of mass number A according to the formula $\hbar\omega_{\text{oscil}} = 1.2 \times \frac{41}{A^{1/3}}$ MeV [81]. These two choices guarantee good convergence of the HFB energy with respect to the basis size, within about 150 keV of the exact value [82].

Pairing correlations were described by the pairing ED (6) with different pairing strengths for protons and neutrons, $V_0^n \neq V_0^p$. As customary for zero-range pairing forces, a cutoff of $E_{\text{cut}} = 60$ MeV is used to truncate the quasiparticle space [73]. To avoid pairing collapse, the Lipkin-Nogami prescription was systematically applied according to Ref. [83].

Taking into account the 13 parameters of the Skyrme EDF and the 2 additional parameters in the pairing channel requires a 15-parameter search. We have made two additional simplifications. First, the tensor coupling constants $C_0^{J^2}$ and $C_1^{J^2}$ were set to 0. This choice was motivated by our requirement to take as a reference point the original SLy4 parameterization of Ref. [18] where these terms were not included. Second, preliminary tests indicated that the isovector effective mass was poorly constrained by our data set. As a result, the obtained values of M_v^* were clearly nonphysical with regard to the discussion in Ref. [84]. In the final run we therefore discarded M_v^* from the list of free parameters and kept the original SLy4 value.

The final optimization was therefore carried on a set of 12 parameters (10 for the Skyrme ED plus 2 pairing strengths):

$$\{\rho_c, E^{\text{NM}}/A, K^{\text{NM}}, a_{\text{sym}}^{\text{NM}}, L_{\text{sym}}^{\text{NM}}, M_s^{*-1}, C_0^{\rho\Delta\rho}, C_1^{\rho\Delta\rho}, V_0^n, V_0^p, C_0^{\rho\nabla J}, C_1^{\rho\nabla J}\}, \tag{42}$$

with $C_0^{J^2} = C_1^{J^2} = 0$ and $M_v^{*-1} = 1.249$.

For scaling purposes, the optimization algorithms tested here require the domain of variation of the various parameters $\mathbf{x}$ to be specified. Because, in practice, a large subset of $\mathbf{x}$ represents symmetric and asymmetric NMPs, the range of variation can be easily set up, even if the exact values are

not known. Table V in Sec. IV A1 lists the scaling intervals adopted in our optimization.

Following the discussion in Sec. II C, our objective function (36) contains $D_T = 3$ data types: nuclear masses ($i = 1$), proton rms radii ($i = 2$), and OES differences ($i = 3$). The total number of data points is $n_d = 108$ and breaks down into $n_1 = 72$ nuclear masses (28 spherical and 44 deformed), $n_2 = 28$ rms proton radii, and $n_3 = 8$ OES differences (4 for neutrons and 4 for protons). The values $d_{i,j}$ of the experimental data points are given in Sec. II C.

The weights w_i in the objective function are used to render all quantities dimensionless and to allow for a composite χ^2 function. The weights must be chosen so that all reduced errors are of the same order of magnitude: They reflect the expected theoretical uncertainty that one can assign to a given observable, which is generally larger than the corresponding experimental uncertainty for our data set. In the optimization described here, we chose $w_{\text{mass}} = 2.0$ MeV, $w_{\text{radii}} = 0.02$ fm, and $w_{\text{OES}} = 50$ keV.

IV. RESULTS

This section contains the optimization results. In Sec. IV A, various properties of the resulting ED parameterizations are explored. Section IV B illustrates the versatility of our approach by providing a detailed correlation and sensitivity analysis.

A. Optimized functionals UNEDFnb and UNEDF0: Properties and stability

We give in this section the final parameterization of the Skyrme functionals UNEDFnb and UNEDF0 that minimizes the χ^2 objective function (36), and we perform a number of checks to probe the quality of the resulting functionals. In particular, we test their stability with the RPA response function, check that both the spherical and deformed shell structure are on par with other parameterizations, and discuss various global performance indicators.

1. Solution to the optimization problem

The optimization of a nuclear energy functional is a complex problem. The objective function is the compound result of many different full HFB calculations, each the result of a self-consistent iterative procedure. In principle, such a function lends itself naturally to parallelization, although the different times of calculation of spherical and deformed configurations requires fine load balancing. Overall, the cost of one function evaluation can typically amount to 10 min on a standard computer cluster. With such costly evaluations, the number of evaluations required to minimize Eq. (36) can rapidly become an issue.

In addition, we have no prior knowledge of the multidimensional surface of the objective function in the parameter space. There is no guarantee that the parameters are all independent, and, as we show later, there are correlations between them, which make the topography of the surface complex.

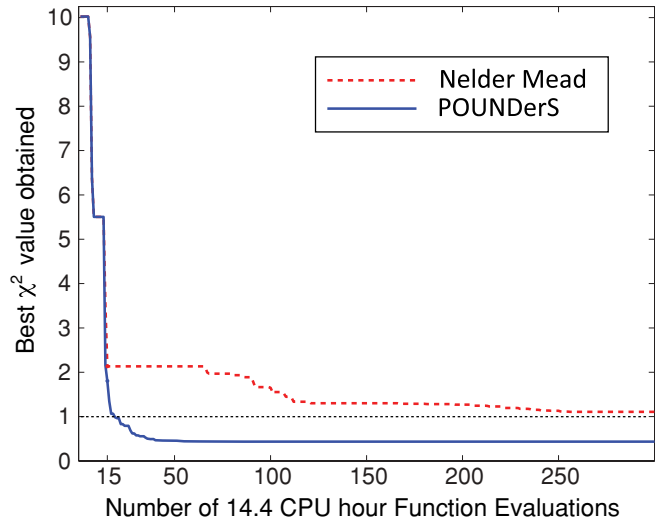

FIG. 2. (Color online) Convergence of the minimization of Eq. (36) with the standard N-M algorithm (dashed line) and the model-based POUNDerS (solid line).

These observations suggest that two important features of a good optimization algorithm should be the speed of convergence and the ability to converge to a true minimum, if only a local one, without being misled by narrow valleys and saddle points. Figure 2 shows the performance of the standard N-M algorithm, as implemented in the TAO code [85], on our objective function, compared with the new model-based algorithm presented in Sec. III A. We note that the POUNDerS method attains a value of χ^2 close to the final one after only 25–30 iterations, whereas after more than 300 iterations the N-M algorithm yields a solution that is still a factor of 2 away. Moreover, there seems to be a stagnation of the N-M method at around 15–65 iterations, which may prematurely suggest that the minimum has been found. Yet, in this plateau the χ^2 is still about 5 times larger than at the final solution.

Table V shows the values of the optimization parameters (42) at the solution (dubbed UNEDFnb in the following). The starting values were given by the SLy4 parameterization. The most notable change affects the effective mass: Starting from $M_s^* \approx 0.7$, the final value is close to 1, which ensures a level density more compatible with the empirical one (even though there is no obvious reason for this to happen, given the data set employed). As will be discussed in Sec. IV A6, without being steered, the optimization gives the correct hierarchy of pairing strengths, namely, $|V_0^p| > |V_0^n|$, to reflect the missing momentum dependence and Coulomb contribution, as pointed out in Refs. [68,86,87].

A standard measure of the quality of the optimization is the rms deviation (RMSD) of data type i at the solution $\hat{\mathbf{x}}$:

$$\text{RMSD}(i) = \sqrt{\frac{1}{n_i}\sum_{j=1}^{n_i}[s_{i,j}(\hat{\mathbf{x}}) - d_{i,j}]^2}. \tag{43}$$

For our set of fit observables, the RMSDs for various types of data are RMSD(mass) = 0.966 MeV, RMSD(radii) = 0.014 fm, and RMSD(OES) = 57 keV. For comparison,

TABLE V. Values $\hat{\mathbf{x}}$ of the optimization parameters $\mathbf{x}$ of Eq. (42) at the solution with no bounds imposed (Skyrme functional UNEDFnb). ρ_c is in fm^{-3}; $E^{\rm NM}/A$, $K^{\rm NM}$, $a_{\rm sym}^{\rm NM}$, and $L_{\rm sym}^{\rm NM}$ are in MeV; $1/M_s^*$ is dimensionless; $C_t^{\rho\Delta\rho}$ and $C_t^{\rho\nabla J}$ are in MeV fm^5; and V_0^n and V_0^p are in MeV fm^3. The range of variation provided to the optimization is shown in the column "Scaling interval," the initial values in column $\hat{\mathbf{x}}^{(\rm init.)}$, and the final values in $\hat{\mathbf{x}}^{(\rm fin.)}$.

k	$\mathbf{x}$	Scaling interval	$\hat{\mathbf{x}}^{(\rm init.)}$	$\hat{\mathbf{x}}^{(\rm fin.)}$
1	ρ_c	[+0.14, +0.18]	+0.160	0.151046
2	$E^{\rm NM}/A$	[−17.00, −15.00]	−15.972	−16.0632
3	$K^{\rm NM}$	[+170.00, +270.00]	+229.901	337.878
4	$a_{\rm sym}^{\rm NM}$	[+27.00, +37.00]	+32.004	32.455
5	$L_{\rm sym}^{\rm NM}$	[+30.00, +70.00]	+45.962	70.2185
6	$1/M_s^*$	[+0.80, +2.00]	+1.439	0.95728
7	$C_0^{\rho\Delta\rho}$	[−100.00, −40.00]	−76.996	−49.5135
8	$C_1^{\rho\Delta\rho}$	[−100.00, +100.00]	+15.657	33.5289
9	V_0^n	[−350.00, −150.00]	−258.200	−176.796
10	V_0^p	[−350.00, −150.00]	−258.200	−203.255
11	$C_0^{\rho\nabla J}$	[−120.00, −50.00]	−92.250	−78.4564
12	$C_1^{\rho\nabla J}$	[−100.00, +50.00]	−30.750	63.9931

the value of RMSD(mass) for SLy4 on the same data set is 9.95 MeV.

A close examination of Table V shows that, while most of the parameters of UNEDFnb have values in the normally accepted range, the incompressibility $K^{\rm NM} = 338$ MeV is far too large. This would seriously limit the usability of UNEDFnb in nuclear structure calculations, in particular in studies of collective modes such as monopole vibrations.

We therefore performed another minimization, using the same scaling intervals, but imposing hard bounds on the NMPs. A similar strategy was adopted in Ref. [88], where hard bounds on $K^{\rm NM}$ were imposed during optimization of BSk13 EDF.

Table VI displays the parameter values of the Skyrme functional UNEDF0 optimized in such a way. At convergence, the nuclear incompressibility and scalar effective mass appear at their respective bounds of 230 MeV and 1.11 ($1/M_s^* = 0.9$); that is, these NMPs are actively constrained. The rms deviations obtained for UNEDF0 on our set of fit observables are still respectable: RMSD(mass) = 1.455 MeV, RMSD(radii) = 0.016 fm, and RMSD(OES) = 59 keV.

TABLE VI. Same as Table V but for the case with bounds (Skyrme functional UNEDF0).

k	$\mathbf{x}$	Bounds	$\hat{\mathbf{x}}^{(\rm init.)}$	$\hat{\mathbf{x}}^{(\rm fin.)}$
1	ρ_c	[+0.15,+0.17]	+0.160	0.160526
2	$E^{\rm NM}/A$	[−16.2,−15.8]	−15.972	−16.0559
3	$K^{\rm NM}$	[+190, +230]	+229.901	230
4	$a_{\rm sym}^{\rm NM}$	[+28, +36]	+32.004	30.5429
5	$L_{\rm sym}^{\rm NM}$	[+40, +100]	+45.962	45.0804
6	$1/M_s^*$	[+0.9, +1.5]	+1.439	0.9
7	$C_0^{\rho\Delta\rho}$	[−∞, +∞]	−76.996	−55.2606
8	$C_1^{\rho\Delta\rho}$	[−∞, +∞]	+15.657	−55.6226
9	V_0^n	[−∞, +∞]	−258.200	−170.374
10	V_0^p	[−∞, +∞]	−258.200	−199.202
11	$C_0^{\rho\nabla J}$	[−∞, +∞]	−92.250	−79.5308
12	$C_1^{\rho\nabla J}$	[−∞, +∞]	−30.750	45.6302

2. *Stability check of* UNEDFnb *and* UNEDF0

It is known that some Skyrme ED parameterizations are prone to finite-size instabilities [84,89–91]. For instance, in the time-even channel, the term $C_1^{\Delta\rho}\rho_1\Delta\rho_1$ can lead to divergences of the HFB iterative procedure. When searching for new functionals, it is therefore crucial to test comprehensively the stability of the functional parameterization. Here, the RPA linear response theory [92] is the tool of choice. The full RPA response in infinite matter has been derived for Skyrme EDFs [93–95], and applications pertaining to the stability of Skyrme functionals have been reported in Refs. [7,84].

Without entering into detail, a general expression for the RPA response function $\Pi(\omega, \mathbf{q})$ in SNM can be written as [92]

$$\Pi(\omega, \mathbf{q}) = \frac{4\Pi_0(\omega, \mathbf{q})}{D(\omega, \mathbf{q})}, \tag{44}$$

where ω is the excitation energy, $\mathbf{q}$ is the transferred momentum (or wave number of the density fluctuation), $\Pi_0(\omega, \mathbf{q})$ is the noninteracting response (or Lindhard function), and $D(\omega, \mathbf{q})$ is the dielectric function, equal to unity in noninteracting SNM.

The value $\Pi(\omega = 0, \mathbf{q})$ corresponds to the static susceptibility of the system to finite-size perturbations. With the preceding sign convention, $\Pi(\omega = 0, \mathbf{q})$ should be positive for all values of $\mathbf{q}$ and the density ρ_0. A change of sign with either variable corresponds to $D(\omega, \mathbf{q}) = 0$; hence, the occurrence of a pole indicating the existence of a zero-energy collective mode. In the isospin channel, the short-wavelength (high-$\mathbf{q}$) behavior is driven essentially by the combination of coefficients $C_1^{\rho\rho} - C_1^{\rho\Delta\rho}q^2$ [60,93]. The magnitude of the latter correlates well with the occurrence of instabilities in calculations of finite nuclei.

Figure 3 shows the dielectric function $D(\omega = 0, \mathbf{q})$ as a function of q, in the scalar-isovector perturbation channel, at

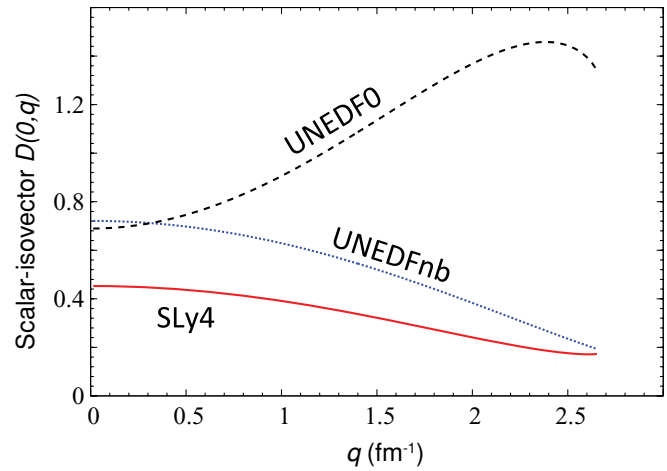

FIG. 3. (Color online) Dielectric function $D(\omega = 0, \mathbf{q})$ for the scalar-isovector channel in SLy4, UNEDF0, and UNEDFnb as a function of the transferred momentum q for $k_F = 1.33$ fm^{-1}.

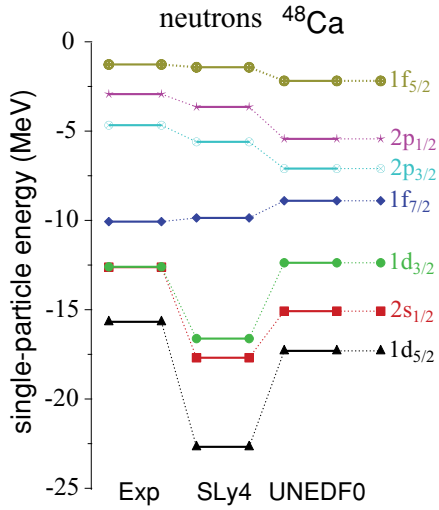

FIG. 4. (Color online) Neutron single-particle energies in ^{48}Ca obtained from a HF calculation with the functional UNEDF0. Experimental s.p. levels [96] and SLy4 results are shown for comparison.

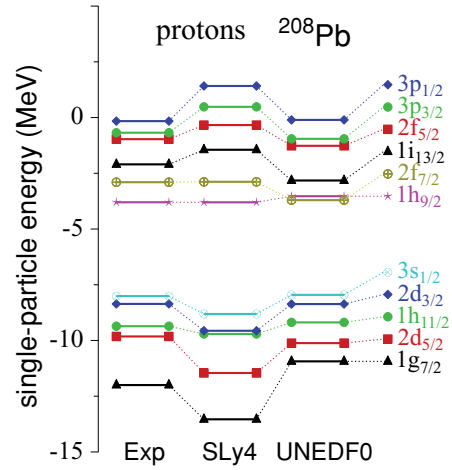

FIG. 5. (Color online) Similar as in Fig. 4 but for proton single-particle energies in ^{208}Pb.

saturation density in SNM. When $D(\omega = 0, \mathbf{q}) = 0$, finite-size instabilities could potentially develop and hinder the usability of the functional. This situation does not occur for UNEDFnb and UNEDF0, which yield a dielectric function even more "stable" than SLy4. Varying the density, we found that the poles of the response function at $\omega = 0$ occur only for $\rho_0 \gtrsim 0.22$ fm^{-3}. This result does not guarantee that other types of instabilities could not develop [91]; however, we can rule out the most common ones.

3. Spherical shell structure

The essence of the nuclear DFT is to be a global theory, whereby one unique functional (or family thereof) should be used to compute with reasonable accuracy various properties of atomic nuclei from the lightest to the heaviest. Many of these properties depend on the single-particle shell structure. Figures 4 and 5 show, respectively, the neutron s.p. energies in ^{48}Ca and proton s.p. energies in ^{208}Pb obtained with UNEDF0. They are compared with levels extracted from experiment [96] and those calculated with SLy4. In ^{208}Pb, the overall agreement of the proton spectrum is very good. Furthermore, the neutron s.p. levels in ^{208}Pb and proton and neutron levels in ^{132}Sn (not shown) agree well with experiment. As seen in Table V, the optimization produces a functional with an effective mass close to 1, which is probably the reason the level density in ^{208}Pb and ^{132}Sn is well reproduced. Although the overall agreement for s.p. energies is good, the systematic effect of high-j states being slightly too high in energy is seen [60].

The neutron single-particle spectrum in ^{48}Ca is, however, poorly reproduced. One of the most alarming features is the absence of the magic gap at $N = 28$ resulting from a large s.p. level density and a reduced spin-orbit splitting. The s.p. proton spectrum of ^{48}Ca is only marginally better with the magic gap at $Z = 20$ being too low, and the situation is similar in ^{40}Ca.

The lack of observables directly probing s.p. properties (such as spin-orbit splittings or shell-gap sizes) in our objective function and the bias on heavy nuclei in the set of fit observables are undoubtedly the main reasons for the poor performance of UNEDF0 regarding the shell structure of light nuclei. Nevertheless, one must bear in mind that even when the optimization is exclusively focused on s.p. properties, standard Skyrme functionals perform poorly [11].

4. Deformation properties

The spherical shell structure determines many features of deformed nuclei. Indeed, the appearance of deformed states and shape coexistence effects can be related to s.p. levels and their couplings through symmetry-violating moments [97,98]. Because the shell structure of light nuclei with UNEDF0 shows large deviations from experiment, it is interesting to test whether the new parameterization can nonetheless produce sensible deformation properties for medium-mass nuclei. To this end, we performed a series of constrained HFB calculations for the sequence of Zr isotopes known to exhibit dramatic shape variations as a function of N. While nuclei near magic ^{90}Zr are known to be spherical, neutron-rich Zr isotopes with $A \geqslant 100$ possess large prolate ground-state deformations, and $^{96-98}$Zr exhibit a complex coexistence pattern [98,99]. On the proton-rich side, there is strong experimental evidence for large prolate deformation in $N = Z = 40$ system ^{80}Zr [98].

Figure 6 shows the evolution of HFB + LN deformation energy in the selected even-even Zr isotopes as a function of the quadrupole deformation β_2. Each point was computed by imposing a constraint on the quadrupole moment $\langle \hat{Q}_2 \rangle \propto \beta_2$. Overall, the energy balance between spherical and deformed configurations is consistent with experiment. In particular, Zr isotopes with $N > 58$ are correctly predicted to have prolate ground states coexisting with a secondary oblate minimum. Also, it is encouraging to see that the ground state of ^{80}Zr is predicted to be prolate, a feature that is not present in many Skyrme parameterizations [98].

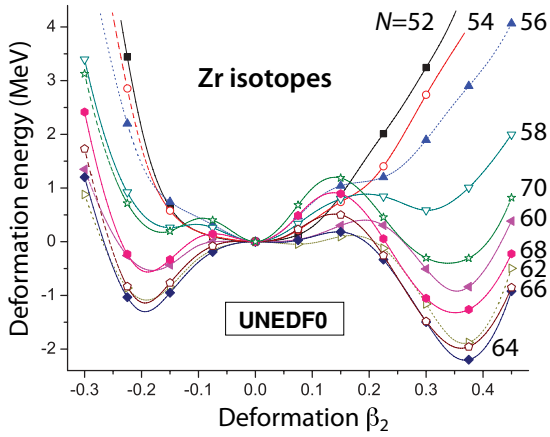

FIG. 6. (Color online) Deformation energy curves as functions of the quadrupole deformation β_2 for selected even-even Zr isotopes calculated in the HFB + LN approach with UNEDF0 Skyrme functional.

5. *Global mass table*

A good test of any EDF parameterization is its ability to reproduce masses across the nuclear chart. Since our objective function contains the binding energies of a large set of nuclei, we expect good agreement with experimental data, especially for heavy deformed systems.

All even-even nuclei with $N, Z > 8$ have been calculated with our two parameterizations according to the method presented in Ref. [9]. Results have been posted for visualization and comparison with other EDF parameterizations at [http://massexplorer.org]. The difference between experimental and theoretical binding energies for the 520 even-even nuclei is shown in Fig. 7. An arclike trend [100] is seen for the SLy4 EDF; it has been attributed to an overemphasis on doubly magic nuclei during optimization. By contrast, both UNEDF0 and UNEDFnb show a much flatter behavior, while simultaneously reducing the mass residuals: RMSD(mass) = 4.80 MeV for SLy4, and 1.45 MeV and 1.61 MeV for UNEDF0 and UNEDFnb, respectively.

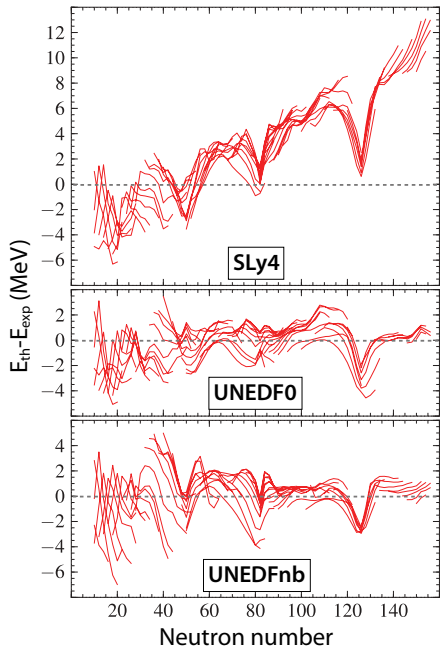

FIG. 7. (Color online) Binding energy residuals between theory and experiment for 520 even-even nuclei. The HFB + LN results with SLy4 (top) are compared with those of UNEDF0 (middle) and UNEDFnb (bottom).

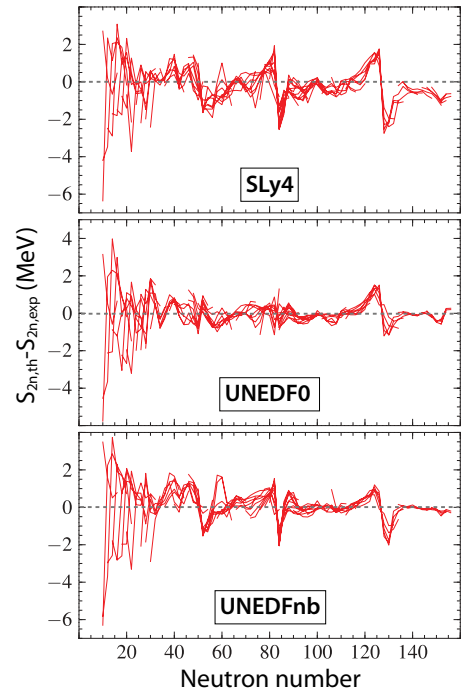

FIG. 8. (Color online) Two-neutron separation energy residuals between theory and experiment for 520 even-even nuclei. The HFB + LN results with SLy4 (top) are compared with those of UNEDF0 (middle) and UNEDFnb (bottom).

To put things in perspective, we note that the best overall agreement with experimental masses obtained with the Skyrme EDF (on a larger data set that includes light and odd nuclei) is currently 0.582 MeV [70]. However, this excellent result was obtained at a price of several corrections on top of the EDF itself. In fact, a linear least-squares refit of the standard Skyrme EDF (also using SLy4 as a starting point) to all even-even nuclear masses achieves a RMSD of around 1.7 MeV [10]. Note also that the RMSD for the masses of the UNEDFnb is higher by a 0.16 MeV than for the UNEDF0 despite the larger domain available for parameter variation, which is attributable to the restricted set of masses used in this work. These figures suggest that UNEDF0 is probably within a few hundreds of keV of a globally optimal mass fit within the parameter space employed here.

Close examination of Fig. 7 reveals that, while the global trend of binding energy errors has been improved, significant variations around that global trend still remain. To quantify this, we plot in Fig. 8 two-neutron separation energy residuals as a function of neutron number N for the 520 nuclei of the previous set. The values of RMSD(S_{2n}) for SLy4 and UNEDF0 are, respectively, 0.99 and 0.76 MeV, which indicate a significant improvement. If the set of 520 nuclei considered

is divided into light ($A < 80$) and heavy ($A \geqslant 80$) subsets, the respective RMSD(S_{2n}) values for SLy4 and UNEDF0 are 1.41 and 1.45 MeV for light nuclei and 0.85 and 0.45 MeV for heavy nuclei. This result stems from the bias toward heavy nuclei in our data set.

6. *Constraints on pairing strength from optimization*

Adjusting pairing interaction strengths represents a situation in which, by sequentially releasing a constraint on the EDF, one can dramatically improve the agreement with a subset of fit observables. The case in point is the interplay between pairing and shell structure. Because the shell correction to the binding energy favors low s.p. level density around the Fermi level, and the opposite is true for pairing contributions, an anticorrelation between these two effects exists that results in a cancellation between shell and pairing energies [101]. If only total binding energies are subject to optimization, a reasonable fit can be obtained by, for example, an unphysical increase in pairing and a simultaneous unphysical variation of s.p. shell structure. Indeed, because no data in our experimental data set directly probe s.p. energies, the lack of constraints on shell structure can dramatically impact pairing properties.

Figure 9 displays the OES residuals for three variants of calculations. In the first variant, the proton and neutron pairing strengths were kept equal and fixed at the standard value for SLy4 that yields an average neutron pairing gap in ^{120}Sn equal to the experimental value of 1.245 MeV [73,74]. In this case, the optimization procedure yields shell structure that resulted in overestimated pairing correlations, and the calculated RMSD for the OEM is 172 keV.

In the next step, we assumed proton and neutron pairing strengths to be identical $V_0^n = V_0^p = V_0$, and the constant V_0

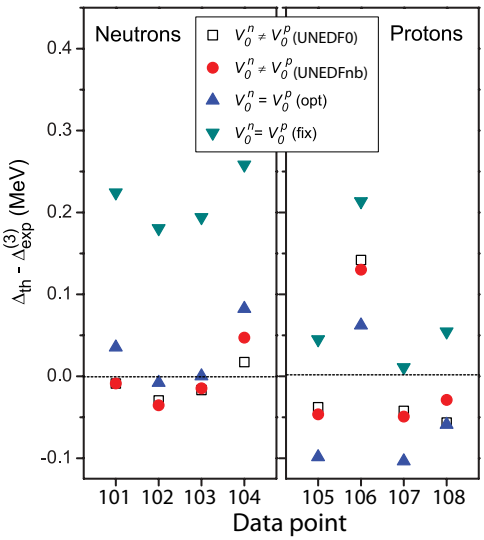

FIG. 9. (Color online) Neutron (left) and proton (right) OES residuals $\Delta_{\rm th} - \Delta^{(3)}_{\rm exp}$ for the nuclei listed in Table IV. The results with fixed (nonoptimized) values of $V_0^n = V_0^p$ are marked with upside-down triangles. The optimized results are marked with triangles ($V_0^n = V_0^p$), dots ($V_0^n \neq V_0^p$; UNEDFnb), and squares ($V_0^n \neq V_0^p$; UNEDF0).

was included in the optimization set. The improvement on pairing energy was immediate, with the rms error on OES dropping down to 67 keV. However, Fig. 9 clearly shows that OES for protons is almost systematically underestimated. This observation calls for using different pairing strengths for neutrons and protons, as was suggested by a recent large-scale survey [68].

Our final optimization run was therefore carried out by considering independent strengths V_0^n and V_0^p in the fit. The rms error on OES has been further reduced to 57 keV in UNEDFnb and 59 keV in UNEDF0, and the two pairing strengths turn out to be significantly different (see Tables V and VI). Apart from possible global physics arguments, this result indicates that this optimization problem benefits from proton and neutron pairing strength being independent parameters.

We conclude this discussion with a word of warning: Strictly speaking, the calculation of the OES requires computation of differences of binding energies. In odd nuclei, time-reversal symmetry is broken, time-odd fields are nonzero, and the ground-state should be computed as the lowest quasiparticle excitation of a fully paired vacuum (blocking). Because the correct blocked state is not known beforehand, such calculations are much more involved than in even-even nuclei [7]. For this work, where the focus is on the optimization of the Skyrme functional itself and the pairing functional is limited, the extra cost of the proper treatment of odd nuclei was not deemed worth pursuing.

B. Statistical analysis of optimization results

From a statistical viewpoint, our optimization problem is also a nonlinear regression problem. For the true (but unknown) parameter value $\mathbf{x}_*$ we define the errors between the theoretical value for the observable of type i in the nucleus j and its experimental counterpart as

$$\varepsilon_{i,j} = \frac{s_{i,j}(\mathbf{x}_*) - d_{i,j}}{w_i}. \tag{45}$$

We assume every error $\varepsilon_{i,j}$ is a random variable with expectation 0 and that all $\varepsilon_{i,j}$ are independent and follow the same distribution. The optimization presented in Sec. III A estimates $\mathbf{x}_*$ by the least-squares estimator

$$\hat{\mathbf{x}} = \arg\min_{\mathbf{x}} \left\{ f(\mathbf{x}) = \tfrac{1}{2}\|\mathbf{F}(\mathbf{x})\|^2 \right\}. \tag{46}$$

In the statistical setting, however, the random errors $\varepsilon = \{\varepsilon_{i,j}\}$ prevent the random variable $\hat{\mathbf{x}}$ from always equaling $\mathbf{x}_*$.

1. *Confidence intervals*

To characterize how the parameters change in a neighborhood of $\mathbf{x}_*$ and $\hat{\mathbf{x}}$, we consider approximate confidence intervals. A $1-\alpha$ *confidence interval* $\Omega_k \subset \mathbb{R}$ is one in which we expect the true value $x_{k,*}$ to lie $100(1-\alpha)\%$ of the time, that is, with probability $P(x_{k,*} \in \Omega_k) = 1-\alpha$.

We note that the assumption of normally distributed residuals, $\varepsilon \sim N(\mathbf{0}, \sigma_*^2 I_{n_d})$, made in what follows, is the strongest one of this regression analysis. As pointed out in Ref. [24], theoretical (systematic) errors coming from an imperfect

model are neither random nor generally independent, and their distribution is not rigorously normal. We carry out a standard analysis nonetheless to investigate constraints applied on our model. Therefore, the confidence intervals given here are to be understood as ranges of acceptable values for building parameterizations of this particular model.

Given normally distributed residuals and appropriate regularity conditions (as in Ref. [102], pages 23–25), a $1-\alpha$ confidence interval (CI) centered about $\hat{x}_k$ is

$$\{x_k \in \mathbb{R} : |x_k - \hat{x}_k| \leqslant \sqrt{\mathrm{Cov}(\hat{\mathbf{x}})_{k,k}}\, t_{n_d-n_x,1-\frac{\alpha}{2}}\}, \qquad (47)$$

where $t_{n_d-n_x,1-\frac{\alpha}{2}}$ is the $1-\frac{\alpha}{2}$ quantile of the t distribution [103] with $n_d - n_x$ degrees of freedom, and the covariance matrix $\mathrm{Cov}(\hat{\mathbf{x}}) = \mathrm{E}[(\hat{\mathbf{x}} - \mathrm{E}\hat{\mathbf{x}})(\hat{\mathbf{x}} - \mathrm{E}\hat{\mathbf{x}})^T]$.

Using the same notation as in Eq. (41), we use a first-order approximation of the covariance matrix,

$$\hat{\mathbf{V}} \equiv \chi^2(\hat{\mathbf{x}}) \left(\sum_{i=1}^{n_d} \mathbf{g}_i \mathbf{g}_i^T \right)^{-1} \approx \mathrm{Cov}(\hat{\mathbf{x}}), \qquad (48)$$

where parameters $\{\mathbf{g}_i\}_{i=1,\ldots,n_d}$ are found by calculating central differences on the $2n_x$ points $\{\hat{\mathbf{x}} \pm \eta_k e_k\}_{k=1,\ldots,n_x}$, where $\eta_k > 0$ is chosen to be small. Although other approximations to the covariance matrix are possible, the authors of Ref. [104] state that $\hat{\mathbf{V}}$ is their preferred approximation because it is "simpler, less expensive, and more numerically stable" than alternative choices.

Tables VII and VIII show the 95% CIs, and standard deviations obtained when η_k is chosen to be 10^{-5} times the size of the scaling interval of parameter x_k. Standard deviations σ are square roots of the diagonal components of the covariance matrix $\mathrm{Cov}(\hat{\mathbf{x}})$ and are often also referred to as errors of parameters.

Confidence intervals can therefore be valuable for testing the completeness of a given data set. In our case no data on giant resonances were included, which may explain why $a_{\mathrm{sym}}^{\mathrm{NM}}$ and $L_{\mathrm{sym}}^{\mathrm{NM}}$ remain imprecise. Similarly, our data set does not contain sufficiently many neutron-rich nuclei and/or entire isotopic sequences to pin down the isovector coupling constants. We also remark that the analysis based on CIs is straightforward to perform once the (computationally intensive) covariance matrix is known.

TABLE VII. Optimal parameter values of UNEDFnb (no bounds), 95% confidence intervals, percentage of the initial guess for the scaling interval, and standard deviation σ.

k	Par.	$\hat{\mathbf{x}}$	95% CI	% of Int.	σ
1	ρ_c	0.151046	[0.149,0.153]	10	0.001
2	E^{NM}/A	−16.0632	[−16.114,−16.013]	5	0.039
3	K^{NM}	337.878	[302.692,373.064]	70	26.842
4	$a_{\mathrm{sym}}^{\mathrm{NM}}$	32.455	[28.839,36.071]	72	2.759
5	$L_{\mathrm{sym}}^{\mathrm{NM}}$	70.2185	[11.108,129.329]	296	45.093
6	$1/M_s^*$	0.95728	[0.832,1.083]	21	0.096
7	$C_0^{\rho\Delta\rho}$	−49.5135	[−55.786,−43.241]	21	4.785
8	$C_1^{\rho\Delta\rho}$	33.5289	[−2.246,69.304]	36	27.292
9	V_0^n	−176.796	[−194.686,−158.906]	18	13.648
10	V_0^p	−203.255	[−217.477,−189.033]	14	10.850
11	$C_0^{\rho\nabla J}$	−78.4564	[−85.137,−71.775]	19	5.097
12	$C_1^{\rho\nabla J}$	63.9931	[23.460,104.526]	54	30.921

TABLE VIII. The same as Table VII, except for the UNEDF0.

k	Par.	$\hat{\mathbf{x}}$	95% CI	% of Int.	σ
1	ρ_c	0.160526	[0.160,0.161]	10	0.001
2	E^{NM}/A	−16.0559	[−16.146,−15.965]	45	0.055
3	K^{NM}	230	–	–	–
4	$a_{\mathrm{sym}}^{\mathrm{NM}}$	30.5429	[25.513,35.573]	126	3.058
5	$L_{\mathrm{sym}}^{\mathrm{NM}}$	45.0804	[−20.766,110.927]	219	40.037
6	$1/M_s^*$	0.9	–	–	–
7	$C_0^{\rho\Delta\rho}$	−55.2606	[−58.051,−52.470]	9	1.697
8	$C_1^{\rho\Delta\rho}$	−55.6226	[−149.309,38.064]	94	56.965
9	V_0^n	−170.374	[−173.836,−166.913]	3	2.105
10	V_0^p	−199.202	[−204.713,−193.692]	6	3.351
11	$C_0^{\rho\nabla J}$	−79.5308	[−85.160,−73.901]	16	3.423
12	$C_1^{\rho\nabla J}$	45.6302	[−2.821,94.081]	65	29.460

2. *Sensitivity analysis*

The covariance matrix depends on the scaling of the parameters; hence, we work with the standard correlation coefficient,

$$R_{k,l} = \frac{\mathrm{Cov}(x_k, x_l)}{\sqrt{\mathrm{Var}(x_k)\mathrm{Var}(x_l)}}, \qquad (49)$$

which captures the (positive or negative) correlation between parameters x_k and x_l. Tables IX and X provide the approximate $n_x \times n_x$ correlation matrix $\mathbf{R}$ calculated when η_k is chosen to be 10^{-5} the size of the interval of interest of parameter x_k, for the solutions UNEDF0 and UNEDFnb, respectively.

Overall, Tables IX and X show that most parameters are interdependent, although the number of significant correlations with $|R_{kk}| \geqslant 0.8$ is small. For UNEDFnb, where all parameters are free, we note that two pairs of NM parameters are well correlated: K^{NM} is 87% correlated with ρ_c [59,105], while $a_{\mathrm{sym}}^{\mathrm{NM}}$ is 97% correlated with $L_{\mathrm{sym}}^{\mathrm{NM}}$ [56,57,106]. The value of the (inverse of the) effective mass appears well correlated with both pairing strengths. We also notice strong correlation between the pairing strengths and the isoscalar spin-orbit coupling constants. Both observations reflect the interplay between single-particle level density and pairing discussed in Sec. IV A6. We also notice that the proton pairing strength is significantly correlated with the neutron pairing strength.

In the case of the UNEDF0 parameterization, K^{NM} and $1/M_s^*$ are removed from the sensitivity analysis. Nevertheless, we note that the various correlations between parameters overall remain, even if they are attenuated compared to the no-bound case.

Next, we illustrate how sensitive the parameters x_k are to the different data types entering χ^2: masses, proton radii, and OES. Here we focus only on the UNEDF0 parameterization, as it is more realistic. We define the $n_x \times n_d$ Jacobian matrix $J(\mathbf{x})$ of the residuals as $J = (\mathbf{g}_1, \ldots, \mathbf{g}_{n_d})$, that is, the matrix formed as the juxtaposition of the n_d column vectors $\mathbf{g}_i$ (n_d

TABLE IX. Correlation matrix (49) for the UNEDFnb parameter set (no bounds).

	ρ_c	E^{NM}/A	K^{NM}	a_{sym}^{NM}	L_{sym}^{NM}	$1/M_s^*$	$C_0^{\rho\Delta\rho}$	$C_1^{\rho\Delta\rho}$	V_0^n	V_0^p	$C_0^{\rho\nabla J}$	$C_1^{\rho\nabla J}$
ρ_c	1.00											
E^{NM}/A	−0.04	1.00										
K^{NM}	−0.87	0.16	1.00									
a_{sym}^{NM}	−0.05	−0.72	−0.29	1.00								
L_{sym}^{NM}	−0.09	−0.62	−0.23	0.97	1.00							
$1/M_s^*$	−0.05	0.05	0.09	−0.10	−0.10	1.00						
$C_0^{\rho\Delta\rho}$	−0.23	0.24	0.34	−0.25	−0.20	−0.86	1.00					
$C_1^{\rho\Delta\rho}$	−0.22	0.29	0.34	−0.65	−0.76	−0.08	0.28	1.00				
V_0^n	0.02	−0.02	−0.06	0.06	0.06	−0.99	0.87	0.12	1.00			
V_0^p	0.01	−0.14	−0.10	0.26	0.27	−0.95	0.78	−0.07	0.93	1.00		
$C_0^{\rho\nabla J}$	0.07	−0.03	0.04	−0.14	−0.17	−0.72	0.78	0.32	0.73	0.65	1.00	
$C_1^{\rho\nabla J}$	−0.07	−0.35	−0.12	0.58	0.66	0.06	−0.26	−0.64	−0.08	0.05	−0.38	1.00

being the number of data, n_x the number of parameters). The $n_x \times n_d$ sensitivity matrix S is

$$S(\mathbf{x}) = [J(\mathbf{x})J^T(\mathbf{x})]^{-1}J(\mathbf{x}). \tag{50}$$

For each line in the sensitivity matrix (each parameter), we can compute the partial sums over each of the three types of data. This computation gives us a measure of the change of the parameter under a global change of all the data of a given type. Figure 10 shows the relative change of parameter x_k when such an *average* datum of an observable is changed. For example, for $i = 1$ (masses), it shows the change in x_k under a variation of all experimental masses.

All of the bars in Fig. 10 have been renormalized to unity, and only relative strengths between mass, radii, and OES data are shown. A large percentage contribution from data type i means that x_k is very sensitive to changes in i, and other data types have little impact on it at the convergence point. As expected, pairing strengths (parameters 9 and 10) are primarily affected by OES data. It is worth noting the very similar sensitivity of the spin-orbit coupling constants (parameters 11 and 12) on all three types of data. Also, nuclear-matter parameters appear to be significantly more dependent on the proton radius than other coupling constants. This is not surprising, considering the relation between the saturation density and the WignerSeitz radius.

The integrated information contained in Fig. 10 cannot assess the impact of a particular data piece on model parameters; hence, a more detailed analysis is needed. To this end, for each experimental observable $d_{i,j}$ (masses, radii, OES), we compute the global change in $\hat{\mathbf{x}}$ as individual data $d_{i,j}$ change (one by one) by $0.1w_i$, namely, 200 keV for masses, 0.002 fm for proton radii, and 50 keV for OES. In this way we can, for instance, evaluate the possible importance of some new experimental observable on a given model [38]. Figure 11 shows the quantity

$$\|\delta\boldsymbol{x}/\sigma\| = \sqrt{\sum_{k=1}^{n_x}\left(\frac{\delta x_k}{\sigma_k}\right)^2}, \tag{51}$$

with δx_k being the change in the value of the parameter x_k under a change of the data $d_{i,j}$, for all $n_d = 108$ data points. This is nothing but the norm of the total change in units of the standard deviation σ_k, defined as before by $\sigma_k = \sqrt{\mathrm{Cov}(x_k, x_k)}$. Large changes in $\hat{\mathbf{x}}$ mean that the parameter values are highly sensitive to the particular value of $d_{i,j}$.

TABLE X. Correlation matrix (49) for the UNEDF0 parameter set.

	ρ_c	E^{NM}/A	K^{NM}	a_{sym}^{NM}	L_{sym}^{NM}	$1/M_s^*$	$C_0^{\rho\Delta\rho}$	$C_1^{\rho\Delta\rho}$	V_0^n	V_0^p	$C_0^{\rho\nabla J}$	$C_1^{\rho\nabla J}$
ρ_c	1.00											
E^{NM}/A	−0.28	1.00										
K^{NM}	–	–	–									
a_{sym}^{NM}	−0.10	−0.88	–	1.00								
L_{sym}^{NM}	−0.17	−0.80	–	0.97	1.00							
$1/M_s^*$	–	–	–	–	–	–						
$C_0^{\rho\Delta\rho}$	0.09	0.80	–	−0.81	−0.74	–	1.00					
$C_1^{\rho\Delta\rho}$	0.20	0.35	–	−0.47	−0.66	–	0.23	1.00				
V_0^n	0.02	0.21	–	−0.23	−0.25	–	0.23	0.23	1.00			
V_0^p	−0.13	−0.42	–	0.52	0.56	–	−0.29	−0.45	−0.14	1.00		
$C_0^{\rho\nabla J}$	0.37	−0.14	–	0.02	−0.00	–	0.44	−0.02	0.09	0.16	1.00	
$C_1^{\rho\nabla J}$	−0.06	−0.18	–	0.27	0.33	–	−0.38	−0.20	−0.01	0.00	−0.37	1.00

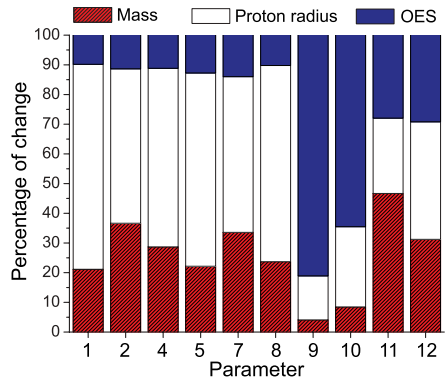

FIG. 10. (Color online) Sensitivity of the parameters of UNEDF0 to different data types entering χ^2. The EDF parameters are labeled as in Table VII.

In principle, the sensitivity analysis can be performed at any point $\mathbf{x}$ of the n_x-dimensional parameter space: For a given scalar function $f(\mathbf{x})$ of the type (36), the sensitivity at point $\mathbf{x}$ is only based on the local gradient. In particular, it is totally independent of the procedure that leads to the specific selection of $\mathbf{x}$. It only depends on the degrees of freedom, that is, free parameters, retained in $f(\mathbf{x})$.

The question of degrees of freedom is highly relevant in the context of the UNEDF0 parameter set, where two parameters are actively constrained at the solution. These constraints have been directly implemented by restricting the domain where the χ^2 function is evaluated, and not by modifying the function by adding a penalty.

The net result of imposing the bound constraints is that only 10 parameters out of 12 are allowed to change near the end of the optimization process. One has, therefore, two options as far as the sensitivity analysis is concerned: (i) Remove these two parameters from the set of active parameters and calculate the Jacobian $J(\mathbf{x})$ and the sensitivity matrix

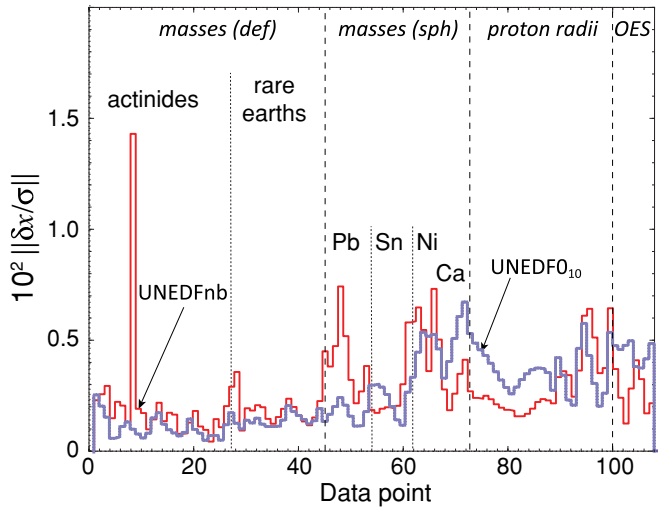

FIG. 11. (Color online) Overall change in $\hat{\mathbf{x}}$ (51) for the UNEDFnb and UNEDF0 parameter sets when data $d_{i,j}$ change by $0.1w_i$ one by one. The labeling of data points is consistent with that in Tables I–IV.

$S(\mathbf{x})$ with only $n_x - 2 = 10$ parameters; (ii) keep all $n_x = 12$ parameters in the calculation of the Jacobian and doing a tangent plan approximation to obtain the relevant covariance and sensitivity matrices. In this way, the uncertainties of the other 10 parameters are affected by the local fluctuations of the surface induced by these two actively constrained parameters.

Alternative (i) boils down to computing the gradient at point $\hat{\mathbf{x}}$ in a 10-parameter subspace of the original 12-parameter space. In this subspace, $\hat{\mathbf{x}}$ is the stable point of the χ^2 function. The curve labeled UNEDF0$_{10}$ in Fig. 11 corresponds to this approach. This sensitivity response is compared with that performed at the free minimum $\hat{\mathbf{x}}^{(\mathrm{nb})}$ of χ^2 in the full 12-parameter space of UNEDFnb. Because both sets correspond to (unconstrained) minima in their respective spaces, the overall changes in $\hat{\mathbf{x}}$ are of the same order of magnitude and they are very small, $\|\delta \boldsymbol{x}/\sigma\| \approx 0.01$. This indicates that the set of fit observables has been chosen very consistently. Indeed, the mass of deformed ^{254}Fm is the single observable that yields the noticeable parameter variations around the UNEDFnb minimum while in the case of UNEDF0$_{10}$ no sensitivity to a single piece of data can be noticed.

By contrast, within alternative (ii), $\hat{\mathbf{x}}$ is not an unconstrained minimizer in the full 12-parameter space. In such an approach, we find the overall sensitivity to be about 2 orders of magnitude larger than what is depicted in Fig. 11. This reflects the fact that x_3 and x_6 are far away from the unconstrained minimum in that space, at the same time being strongly correlated with other parameters. In this case, the sensitivities depend strongly on the actual value of $\hat{\mathbf{x}}$ and the way the domain is constrained. For this reason, option (ii) is of no practical interest in the comparison with the no-bounds results.

V. CONCLUSIONS

One of the major challenges for the low-energy nuclear theory is to construct the global nuclear EDF of spectroscopic quality, rooted in microscopic theory. An important element of this program is to optimize the parameters of the functional on a set of experimental observables and selected theoretical pseudodata. This work shows how such an optimization can be done by using modern optimization algorithms and nonlinear regression analysis.

The purpose of this study was to optimize the standard Skyrme functional based on a set of experimental data (masses, charge radii, and odd-even mass differences) pertaining to 72 spherical and deformed nuclei amenable to a mean-field description. The new model-based optimization algorithm POUNDerS was compared with other standard derivative-free optimization methods such as Nelder-Mead and was found to be significantly better in terms of speed, accuracy, and precision.

The optimization was carried out at the fully self-consistent, deformed HFB level. Here, we took advantage of the efficient DFT solver HFBTHO optimized in the first phase of the project. We have implemented various improvements that enable us to quickly compute global self-consistent mass tables. This capability is essential for optimization.

As a result of the 12-parameter optimization of Skyrme EDF, we arrived at two solutions. The first one corresponds to a minimum (stable point) in the considered parameter space. The corresponding functional UNEDFnb describes well the assumed set of fit observables, but its incompressibility parameter is too large, as this property has not been well constrained by our data set. The second optimization was carried out assuming hard bounds on the nuclear-matter parameters. For the bound-constrained solution, the nuclear incompressibility and scalar effective mass appear at their respective bounds. The resulting parameter set UNEDF0 gives good agreement with experimental masses, radii, and deformations and seems to be free of finite-size instabilities. In particular, for two-neutron separation energies and masses of even-even heavy nuclei with $A > 80$, UNEDF0 yields the rms deviation of 0.45 and 1.2 MeV, respectively, which is a satisfying result. We emphasize that the original Skyrme EDFs seem to be inherently limited in this respect, as demonstrated in Ref. [10], unless specific corrections are introduced. Our result is therefore in line with the best expectations one could have for such EDFs. Nevertheless, the lack of specific constraints on the shell structure in our data set implies that single-particle levels of light nuclei are not well reproduced. For that reason, UNEDF0 may not yet be recommended for truly global applications across the chart of the nuclides. However, this functional is expected to work well for heavy nuclei and should be considered as a reference against which more advanced EDFs will be benchmarked.

We have also applied full-fledged regression diagnostics on UNEDFnb and UNEDF0, focusing on statistical correlations between ED parameters and the sensitivity of parameters to variations in fit observables. To this end, we computed and analyzed the correlation and sensitivity matrices at the optimal parameter set. This kind of nonlinear regression analysis is expected to be helpful when designing next-generation EDFs. Moreover, the statistical tools presented in this study can be used to pinpoint specific nuclear observables that are expected to strongly affect the developments of the nuclear universal density functional.

ACKNOWLEDGMENTS

We thank Peter Klüpfel for his help with the experimental database used in this work. This work was supported by the Office of Nuclear Physics, US Department of Energy under Contracts No. DE-FC02-09ER41583 (UNEDF SciDAC Collaboration), No. DE-FG02-96ER40963 and No. DE-FG02-07ER41529 (University of Tennessee), No. DE-FG0587ER40361 (Joint Institute for Heavy Ion Research), and No. DE-AC0Z-06CA11357 (Argonne National Laboratory). Computational resources were provided through an INCITE award "Computational Nuclear Structure" by the National Center for Computational Sciences and National Institute for Computational Sciences at Oak Ridge National Laboratory and through an award by the Laboratory Computing Resource Center at Argonne National Laboratory.

[1] *Research Facilities in Nuclear Physics*, IUPAP Report 41.
[2] *RIA Theory Bluebook: A Road Map* [http://fribusers.org].
[3] Top 500 [http://www.top500.org].
[4] G. F. Bertsch, D. J. Dean, and W. Nazarewicz, SciDAC Review, Winter 2007, p. 42.
[5] M. Bender, P.-H. Heenen, and P.-G. Reinhard, Rev. Mod. Phys. **75**, 121 (2003).
[6] M. V. Stoitsov, J. Moré, W. Nazarewicz, J. C. Pei, J. Sarich, N. Schunck, A. Staszczak, and S. Wild, J. Phys. Conf. Ser. **180**, 012082 (2009).
[7] N. Schunck, J. Dobaczewski, J. McDonnell, J. Moré, W. Nazarewicz, J. Sarich, and M. V. Stoitsov, Phys. Rev. C **81**, 024316 (2010).
[8] M. V. Stoitsov, J. Dobaczewski, W. Nazarewicz, and P. Borycki, Int. J. Mass Spectrom. **251**, 243 (2006).
[9] M. V. Stoitsov, W. Nazarewicz, N. Schunck, Int. J. Mod. Phys. E **18**, 816 (2009).
[10] G. F. Bertsch, B. Sabbey, and M. Uusnäkki, Phys. Rev. C **71**, 054311 (2005).
[11] M. Kortelainen, J. Dobaczewski, K. Mizuyama, and J. Toivanen, Phys. Rev. C **77**, 064307 (2008).
[12] J. E. Drut, R. J. Furnstahl, and L. Platter, Prog. Part. Nucl. Phys. **64**, 120 (2010).
[13] B. Gebremariam, T. Duguet, and S. K. Bogner, arXiv:0910.4979 [nucl-th].
[14] B. Gebremariam, S. K. Bogner, and T. Duguet, arXiv:1003.5210 [nucl-th].
[15] B. G. Carlsson and J. Dobaczewski, arXiv:1003.2543 [nucl-th].
[16] B. G. Carlsson, J. Dobaczewski, and M. Kortelainen, Phys. Rev. C **78**, 044326 (2008).
[17] B. G. Carlsson, J. Dobaczewski, J. Toivanen, and P. Vesely, Comp. Phys. Commun. **181**, 1641 (2010).
[18] E. Chabanat, P. Bonche, P. Haensel, J. Meyer, and R. Schaeffer, Phys. Scr. T **56**, 231 (1995).
[19] J. Dechargé and D. Gogny, Phys. Rev. C **21**, 1568 (1980).
[20] J.-F. Berger, M. Girod, and D. Gogny, Comput. Phys. Commun. **63**, 365 (1991).
[21] F. Chappert, M. Girod, and S. Hilaire, Phys. Lett. B **668**, 420 (2008); F. Chappert, Ph.D. thesis, Université de Paris-Sud XI, 2007 [http://tel.archives-ouvertes.fr/tel-00177379/en/].
[22] T. Bürvenich, D. G. Madland, J. A. Maruhn, and P.-G. Reinhard, Phys. Rev. C **65**, 044308 (2002).
[23] T. Nikšić, D. Vretenar, and P. Ring, Phys. Rev. C **78**, 034318 (2008).
[24] J. Toivanen, J. Dobaczewski, M. Kortelainen, and K. Mizuyama, Phys. Rev. C **78**, 034306 (2008).
[25] P. Klüpfel, P.-G. Reinhard, T. J. Burvenich, and J. A. Maruhn, Phys. Rev. C **79**, 034310 (2009).
[26] J. Bartel, P. Quentin, M. Brack, C. Guet, and H. B. Håkansson, Nucl. Phys. A **386**, 79 (1982).
[27] F. Tondeur, S. Goriely, J. M. Pearson, and M. Onsi, Phys. Rev. C **62**, 024308 (2000).
[28] S. Goriely, M. Samyn, and J. M. Pearson, Phys. Rev. C **75**, 064312 (2007).
[29] T. Duguet and J. Sadoudi, J. Phys. G **37**, 064009 (2010).
[30] J. A. Sheikh and P. Ring, Nucl. Phys. A **665**, 71 (2000).

[31] J. A. Sheikh, P. Ring, E. Lopes, and R. Rossignoli, Phys. Rev. C **66**, 044318 (2002).
[32] M. V. Stoitsov, J. Dobaczewski, R. Kirchner, W. Nazarewicz, and J. Terasaki, Phys. Rev. C **76**, 014308 (2007).
[33] J. Dobaczewski, J. Phys. G **36**, 105105 (2009).
[34] D. Lacroix, T. Duguet, and M. Bender, Phys. Rev. C **79**, 044318 (2009).
[35] T. Duguet, M. Bender, K. Bennaceur, D. Lacroix, and T. Lesinski, Phys. Rev. C **79**, 044320 (2009).
[36] M. Bender, T. Duguet, and D. Lacroix, Phys. Rev. C **79**, 044319 (2009).
[37] J. Friedrich and P.-G. Reinhard, Phys. Rev. C **33**, 335 (1986).
[38] P.-G. Reinhard and W. Nazarewicz, Phys. Rev. C **81**, 051303 (2010).
[39] P. Ring and P. Schuck, *The Nuclear Many-Body Problem* (Springer-Verlag, Berlin, 1980).
[40] E. Perlińska, S. G. Rohoziński, J. Dobaczewski, and W. Nazarewicz, Phys. Rev. C **69**, 014316 (2004).
[41] Y. M. Engel, D. M. Brink, K. Goeke, S. J. Krieger, and D. Vautherin, Nucl. Phys. A **249**, 215 (1975).
[42] J. Dobaczewski, W. Nazarewicz, and M. V. Stoitsov, Eur. Phys. J. A **15**, 21 (2002).
[43] E. Chabanat, P. Bonche, P. Haensel, J. Meyer, and R. Schaeffer, Nucl. Phys. A **627**, 710 (1997).
[44] J. R. Stone and P.-G. Reinhard, Prog. Part. Nucl. Phys. **58**, 587 (2007).
[45] J. Piekarewicz, J. Phys. G **37**, 064038 (2010).
[46] J. P. Blaizot, Phys. Rep. **64**, 171 (1980).
[47] G. Colò, N. V. Giai, J. Meyer, K. Bennaceur, and P. Bonche, Phys. Rev. C **70**, 024307 (2004).
[48] B. G. Todd-Rutel and J. Piekarewicz, Phys. Rev. Lett. **95**, 122501 (2005).
[49] B. A. Brown, Phys. Rev. C **58**, 220 (1998).
[50] W. Zuo, I. Bombaci, and U. Lombardo, Phys. Rev. C **60**, 024605 (1999).
[51] W. Zuo, A. Lejeune, U. Lombardo, and J. F. Mathiot, Eur. Phys. J. A **14**, 469 (2002).
[52] E. N. E. van Dalen, C. Fuchs, and A. Faessler, Phys. Rev. Lett. **95**, 022302 (2005).
[53] K. Hebeler, T. Duguet, T. Lesinski, and A. Schwenk, Phys. Rev. C **80**, 044321 (2009).
[54] S. Goriely, M. Samyn, M. Bender, and J. M. Pearson, Phys. Rev. C **68**, 054325 (2003).
[55] B. Li, L. Chen, and C. Ko, Phys. Rep. **464**, 113 (2009).
[56] F. Tondeur, M. Brack, M. Farine, and J. M. Pearson, Nucl. Phys. A **420**, 297 (1984).
[57] P.-G. Reinhard, M. Bender, W. Nazarewicz, and T. Vertse, Phys. Rev. C **73**, 014309 (2006).
[58] L. W. Chen, C. M. Ko, and B. A. Li, Phys. Rev. C **72**, 064309 (2005).
[59] L. W. Chen, B. J. Cai, C. M. Ko, B. A. Li, C. Shen, and J. Xu, Phys. Rev. C **80**, 014322 (2009).
[60] T. Lesinski, M. Bender, K. Bennaceur, T. Duguet, and J. Meyer, Phys. Rev. C **76**, 014312 (2007).
[61] [http://orph02.phy.ornl.gov/workshops/lacm08/UNEDF/database.html].
[62] G. Audi, A. H. Wapstra, and C. Thibault, Nucl. Phys. A **729**, 337 (2003).
[63] M. Beiner, H. Flocard, N. Van Giai, and P. Quentin, Nucl. Phys. A **238**, 29 (1975).
[64] M. Zalewski, J. Dobaczewski, W. Satuła, and T. R. Werner, Phys. Rev. C **77**, 024316 (2008).
[65] G. Audi and A. H. Wapstra, Nucl. Phys. A **595**, 409 (1995); **565**, 1 (1993).
[66] G. Fricke, C. Bernhardt, K. Heilig, L. A. Schaller, L. Schellenberg, E. B. Shera, and C. W. De Jager, At. Data Nucl. Data Tables **60**, 177 (1995).
[67] C. Amsler *et al.* (Particle Data Group), Phys. Lett. B **667**, 1 (2008).
[68] G. F. Bertsch, C. A. Bertulani, W. Nazarewicz, N. Schunck, and M. V. Stoitsov, Phys. Rev. C **79**, 034306 (2009).
[69] L. G. Cao, U. Lombardo, and P. Schuck, Phys. Rev. C **74**, 064301 (2006).
[70] S. Goriely, N. Chamel, and J. M. Pearson, Phys. Rev. Lett. **102**, 152503 (2009).
[71] W. Satuła, J. Dobaczewski, and W. Nazarewicz, Phys. Rev. Lett. **81**, 3599 (1998).
[72] J. Dobaczewski, P. Magierski, W. Nazarewicz, W. Satuła, and Z. Szymański, Phys. Rev. C **63**, 024308 (2001).
[73] J. Dobaczewski, H. Flocard, and J. Treiner, Nucl. Phys. A **422**, 103 (1984).
[74] J. Dobaczewski, W. Nazarewicz, and T. R. Werner, Phys. Scr. T **56**, 15 (1995).
[75] T. Kolda, R. M. Lewis, and V. Torczon, SIAM Rev. **45**, 385 (2003).
[76] David E. Goldberg, *Genetic Algorithms in Search, Optimization, and Machine Learning* (Addison-Wesley, Reading, MA, 1989).
[77] J. J. Moré and S. M. Wild, SIAM J. Optim. **20**, 172 (2009).
[78] S. M. Wild, A Derivative-Free Optimization Algorithm Using Minimal Norm Hessians, *Tenth Copper Mountain Conference on Iterative Methods* (2008).
[79] A. R. Conn, K. Scheinberg, and L. N. Vicente, *Introduction to Derivative-Free Optimization* (Society for Industrial and Applied Mathematics, Philadelphia, 2009), MPS/SIAM Series on Optimization.
[80] M. V. Stoitsov, J. Dobaczewski, W. Nazarewicz, and P. Ring, Comput. Phys. Commun. **167**, 43 (2005).
[81] J. Dobaczewski and J. Dudek, Comput. Phys. Commun. **102**, 166 (1997); **102**, 183 (1997).
[82] J. C. Pei, M. V. Stoitsov, G. I. Fann, W. Nazarewicz, N. Schunck, and F. R. Xu, Phys. Rev. C **78**, 064306 (2008).
[83] M. V. Stoitsov, J. Dobaczewski, W. Nazarewicz, S. Pittel, and D. J. Dean, Phys. Rev. C **68**, 054312 (2003).
[84] T. Lesinski, K. Bennaceur, T. Duguet, and J. Meyer, Phys. Rev. C **74**, 044315 (2006).
[85] J. Moré, T. Munson, S. Benson, L. Curfman McInnes, and J. Sarich, *Tao User Manual* (revision 1.9) (Mathematics and Computer Science Division, Argonne National Laboratory, Argonne, IL, 2007), Technical Report ANM/MCS-TM-242 [http://www.mcs.anl.gov/tao].
[86] M. Anguiano, J. L. Egido, and L. M. Robledo, Nucl. Phys. A **696**, 467 (2001).
[87] T. Lesinski, T. Duguet, K. Bennaceur, and J. Meyer, Eur. Phys. J. A **40**, 121 (2009).
[88] S. Goriely, M. Samyn, and J. M. Pearson, Nucl. Phys. A **773**, 279 (2006).
[89] J. P. Blaizot, Phys. Lett. B **60**, 435 (1976).
[90] E. Caurier and B. Grammaticos, Phys. Lett. B **92**, 236 (1980).
[91] M. Kortelainen and T. Lesinski, J. Phys. G **37**, 064039 (2010).
[92] A. L. Fetter and J. D. Walecka, *Quantum Theory of Many-Particle Systems* (McGraw-Hill, Boston, 1971).

[93] C. García-Recio, J. Navarro, N. Van Giai, and L. L. Salcedo, Ann. Phys. **214**, 293 (1992).
[94] J. Margueron, J. Navarro, and N. Van Giai, Phys. Rev. C **74**, 015805 (2006).
[95] D. Davesne, M. Martini, K. Bennaceur, and J. Meyer, Phys. Rev. C **80**, 024314 (2009).
[96] N. Schwierz, I. Wiedenhover, and A. Volya, arXiv:0709.3525.
[97] J. L. Wood, K. Heyde, W. Nazarewicz, M. Huyse, and P. van Duppen, Phys. Rep. **215**, 101 (1992).
[98] P.-G. Reinhard, D. J. Dean, W. Nazarewicz, J. Dobaczewski, J. A. Maruhn, and M. R. Strayer, Phys. Rev. C **60**, 014316 (1999).
[99] J. Skalski, S. Mizutori, and W. Nazarewicz, Nucl. Phys. A **617**, 282 (1997).
[100] J. Dobaczewski, M. V. Stoitsov, W. Nazarewicz, AIP Conf. Proc. **726**, 51 (2004).
[101] W. Nazarewicz, Nucl. Phys. A **574**, 27c (1994).
[102] George A. F. Seber and C. J. Wild, *Nonlinear Regression* (Wiley, New York, 1989).
[103] D. C. Montgomery and G. C. Runger, *Applied Statistics and Probability for Engineers* (Wiley & Sons, New York, 2003).
[104] J. R. Donaldson and R. B. Schnabel, Technometrics **29**, 67 (1987).
[105] B. Cochet, K. Bennaceur, P. Bonche, T. Duguet, and J. Meyer, Nucl. Phys. A **731**, 34 (2004).
[106] M. Warda, X. Viñas, X. Roca-Maza, and M. Centelles, Phys. Rev. C **80**, 024316 (2009).